Distributed Control Systems for a Wastewater Treatment Plant: Architectures and Advanced Control Solutions

Dan Selișteanu, Ion Marian Popescu, Emil Petre,
Monica Roman, Dorin Șendrescu and Bogdan Popa

Additional information is available at the end of the chapter

http://dx.doi.org/10.5772/intechopen.74827

Abstract

This chapter is focused on the development and implementation of a distributed and hierarchized control system for the wastewater treatment plant (WTP) Calafat, Romania. The primary control loops for both treatment lines (water and activated sludge) are developed and analyzed. Also, the distributed control system (DCS) architecture of the wastewater treatment plant is presented, and the advantages of the proposed control structure are highlighted. In order to increase the performance of the overall control system, some advanced control solutions are investigated. More precisely, multivariable adaptive and robust control algorithms are proposed for the activated sludge bioprocess. Several realistic simulation experiments are performed, and the obtained results are analyzed.

Keywords: wastewater treatment, activated sludge, control systems, distributed control, adaptive control

1. Introduction

In this chapter, a control architecture developed at the wastewater treatment plant (WTP) Calafat (located in Oltenia region, Romania) is presented. This control structure was developed in the frame of research project ADCOSBIO (no. 211/2014, UEFISCDI) [1] and contract no. 168/2017, University of Craiova-Water Company Oltenia (WCO). More precisely, a distributed control system (DCS)-supervisory control and data acquisition (SCADA) architecture was proposed, which is organized as a distributed and hierarchized control system. This control solution envisaged the wastewater treatment plant Calafat but can be adapted and implemented for other similar wastewater treatment plants from the WCO.

The wastewater treatment is a process operated to convert wastewater into an effluent that can be returned to the water cycle with minimal impact on the environment. This process takes place in a wastewater treatment plant (WTP) [2]. In a WTP, the treatment usually comprises three stages, called primary, secondary, and tertiary treatments [3]. Primary treatment consists in the mechanical removing of settled and floating materials, and the remaining liquid can be discharged or directed to secondary treatment. Secondary treatment removes dissolved and suspended biological matter, and it is typically performed by microorganisms in a special habitat. The goal of tertiary treatment is to provide a final treatment stage to improve the effluent quality before it is released to the environment. The treatment method used at the WTP Calafat is a classical one, with a mechanical stage for the impurity removal and a biological stage based on activated sludge. The proposed control solution for this WTP is based on a DCS structure.

The paradigm of DCSs is related to the control of medium and high complexity processes, and it consists in the implementation of distributed and hierarchized systems in a number of four to five levels [4]. The two main attributes of the DCS should be mentioned here: the horizontal functionality in each level is managed by a real-time operating system, and the communication between levels is characterized by the network used in the DCS. Currently, some modern technologies from the networks and processing devices are incorporated into the DCSs [5, 6]. The DCS-SCADA solution for the WTP Calafat consists in four levels: the field level (level 0), the direct control level (level 1), the plant supervisory level (level 2), and the production control/regional coordination level (level 3). In this chapter, the structure of the first three levels and their functionality are presented. The primary control loops implemented at level 1 of DCS-WTP Calafat are described. Also, due to the fact that the performance improvement of the WTP control system is possible only by managing the activated sludge bioprocess, some advanced control solutions based on nonlinear adaptive and robust control algorithms are proposed for level 2 of the DCS.

The activated sludge process implemented at WTP Calafat is an aerobic process, highly nonlinear and characterized by parametric uncertainties [3, 7–11]. The best-known model that tries to describe the activated sludge processes is ASM1 (Activated Sludge Model No. 1) [3, 10–12]. The main drawback of ASM1 is its complexity, such that it becomes unfeasible for control. Thus, in this chapter a simplified model of the activated sludge process will be used. The model is based on the model of Nejjari et al. [8], adapted for WTP Calafat.

Several control strategies were developed for bioprocesses, such as linearizing strategy, adaptive approach [3, 7–9], robust and optimal control, sliding mode control [13], model predictive control [14], etc. Yet, in all these schemes, the knowledge of all inputs is required. Unfortunately, for wastewater treatment processes, usually, the complete knowledge of inputs is not available. For these cases, interval observers (or set observers) were developed in the last period, allowing the reconstruction of a guaranteed interval for the unmeasured states instead of estimating their precise numerical values. The only requirement is to know an interval in which the unmeasured inputs of the process evolve. These robust observers are capable of coping with the problems posed by both the uncertainties in the inputs and the incomplete knowledge of process kinetics [15–18].

In this chapter, some of our previous results [12] are extended for WTP Calafat in order to design multivariable adaptive and robust control algorithms. The proposed control strategies are able to handle the model uncertainties of an activated sludge process used for removal of two pollutants carried out in a continuous recycle reactor. The main control objective is to maintain the pollution level at a desired low value despite the load and concentration variations of the pollutant. The adaptive control scheme is designed by combining a linearizing control law with a state asymptotic observer and with an estimator used for online estimation of unknown kinetics. The robust control structure is designed as a linearizing control law plus an interval observer able to estimate lower and upper bounds in which the unmeasured states are guaranteed to lie. Moreover, the uncertain process parameters are replaced by their lower and upper bounds assumed known.

The chapter is organized as follows. In Section 2, the general characteristics of the WTP Calafat and the process flow are presented. Section 3 proposes a distributed control solution for the wastewater treatment process from WTP Calafat. The control architecture and the primary control loops are analyzed. In Section 4, the design of multivariable adaptive and robust control schemes for the activated sludge process is provided. The behavior of the proposed control algorithms is analyzed by performing realistic simulation experiments. The final conclusions are presented in Section 5.

2. Description of the technological process flow

The general characteristics of the wastewater treatment plant (WTP) Calafat and the process flow will be presented. The process flow comprises two stages: the pretreatment (which is the so-called mechanical stage) and the biological stage. **Figure 1** presents the general block diagram of the WTP, and **Figure 2** shows an aerial photography of the WTP.

The WTP was designed for the treatment of a daily average flow of 8366 m^3/day and of a maximum flow of 530 m^3/h. The WTP size was chosen in order to solve the needs of a number of maximum 29,000 inhabitants of Calafat town, predicted for 2020. The treatment method is a classical one, with a mechanical stage for the impurity removal and a biological stage based on activated sludge. The wastewater enters in a tank; it is lifted with special pumps to the pretreatment area and after that is gravitationally discharged in the biological tanks, where the water is aerated and mixed with the activated sludge. Thus, the biodegradation of the water occurs. Finally, the effluent is discarded through decantation.

2.1. Process flow: pretreatment

The process technological lines will be succinctly described. After the entering in the WTP, the influent wastewater passes through a bar screen (the gross filter) to remove all large objects, and after that it flows in a gravitationally way through a slit in the pump room. This unit is

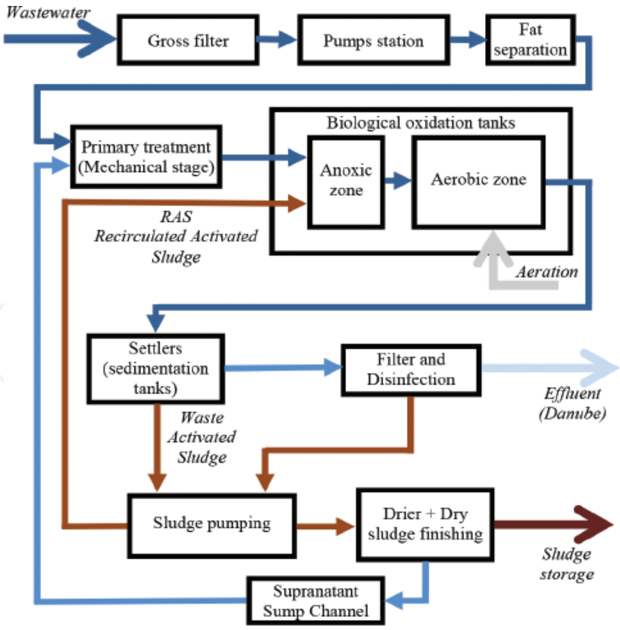

Figure 1. Block diagram (WTP Calafat).

Figure 2. WTP Calafat (aerial photo).

equipped with three Flygt submersible centrifugal pumps P1.A, P1.B, and P1.S (two active pumps (A and B) and one for backup (S)). The water level is measured by using an ultrasonic transducer L1 and is kept between two limits (preestablished limits depending on average water flow). By using the level information, the pumps act to keep the level into the limits. Also, the level information is transmitted to the process computer in the central control room. The water exits from the pumps P1.A, P1.B, and P1.S through three vertical pipes, which at the superior part of the tank (in the valve room) pass to a horizontal configuration and after that merge into a collector. From the valve room, a pipeline goes to the preliminary treatment (pretreatment: mechanical stage). This plant is placed on a metallic structure at the +6.40 m elevation.

An electromagnetic flow meter is placed on the vertical part of the pipe, and it is used to measure the hourly flow of the wastewater provided by the pumps P1.A, P1.B, and P1.S. By opening two sluice valves located at the entrance of the channels used for thin filtering, the wastewater resulted from the pumps P1.A, P1.B, and P1.S passes through the channels and is filtrated by using some rotational filters. The thin impurities which are separated by the filters are then discharged on a conveyer belt and stored into a special tank.

The wastewater enters in a tangential manner in the workers, and, under the mixer action, the water has a descendant spiral movement. After that, the wastewater is lifted through a central pipe, and finally it is evacuated through a radial pipe. This movement, due to the gravitational and centrifugal forces, allows the sedimentation of the solids in the lower part of the workers. The fat and grease floating on the surface are collected by the skimmers. The solid particles are removed by opening the sliding valves, and thus these particles are periodically drained via a spiral conveyer. The grit is cleared into a special tank. After the pretreatment, the water passes via a pipeline which ramifies at the superior part of the biological tanks in the anoxic zones.

2.2. Process flow: biological stage

The biological tanks consist of two biological reactors (bioreactors) and two settlers (sedimentation tanks). These are circular tanks, positioned in a concentric manner, with the settler in the inner part and the biological reactor in the exterior. The walls of the tanks (5 m height) are from special glassed steel. The walls are embedded into concrete structures plated with Izocor hydro-isolation. The external diameter is $d_1 = 35.16$ m, the volume is $V = 3800$ m^3, and the inner diameter is $d_2 = 18.86$ m. At the biological reactor, the bottom is plane, but the bottom of the settler is in the shape of a truncated cone. The bioreactor is divided in two zones, anoxic and aerobic, by using two steel walls, radially disposed. The ratio of the volumes is 30% anoxic/70% aerobic.

In the anoxic zone of each bioreactor, the wastewater from the pretreatment is mixed with the activated sludge which is recirculated by the Flygt pumps RAS/SAS P3.A, P3.B, P3.S. These pumps are controlled with frequency converters, and the flow ratio is 1:1. An equal flow of mixture from the aerobic zone is pumped through a slit from the zone separation wall by the internal recirculation pumps P2.A and P2.B (Flygt type, with frequency converters). The mixers placed in this anoxic zone achieve the homogenization of the three inputs (wastewater, activated sludge, aerobic mixture). In the anoxic zone, the next actions are achieved:

- An appropriate ratio between the substrate (the organic content of the wastewater + nutrients) and the microorganisms (the active content of the sludge)
- The denitrification process (the nitrogen removal)

From the anoxic zone, the compound passes into the aerobic zone, where the biochemical oxidation of the organic matter is achieved. The needed oxygen is provided from the air delivered by the BOC Edwards air blowers A1.A, A1.B, and A1.S and bubbled as thin bubbles by using polymeric membranes. Two technological variables are very important for the aerobic process: the dissolved oxygen (DO) and the pH of the mixture. These are measured and indicated by using the transducers Q1 and Q2 (for DO concentration) and Q3 and Q4, respectively, (for pH). The air is blown by the air blowers A1.A, A1.B, and A1.S (two active and one for backup) through galvanized steel pipes. The air pressure and temperature can be monitored by using the local devices. The airflows at the two tanks are measured by using the flow meters F1 and F2. The flow control is necessary in order to maintain the DO concentration between the specified values. The DO is measured by using the sensors Q1 and Q2, and the information is used to control the air blower speed by using frequency converters.

The mixture from the aerobic zone arrives at the partition wall where one-third from the flow is taken by the recirculation pumps P2.A and P2.B and delivered to the anoxic zones and two-thirds from the flow is passed through a pipeline (via the communicating vessel principle) into the central pipe of the settler. From here the mixture exits in a radial and uniform way at the superior part. The effluent is separated from the sludge and after that is gravitationally removed through a circular drain. Finally, the effluent is flushed in the Danube through a channel. The settlers are equipped with radial scrapper bridges, which have a double goal:

- The superior scrapper collects the foam and directs it to a foam-collecting chamber.
- The inferior scrapper cleans the sediments and directs the sludge to a discharge whirl.

The activated sludge is transported to a collector from which is exhausted through three ramifications by the pumps RAS/SAS P3.A, P3.B, P3.S (RAS is the recirculated activated sludge at the anoxic zones; SAS is the surplus activated sludge, which is carried to a special tank).

As a conclusion, in the biological tanks, the following processes occur:

- The decomposition of the organic matters by using enzymes (enzymatic reactions)
- Assimilation of some components by the microorganisms
- Microorganism growth (increase of the activated sludge mass)
- Oxygen consumption for endogenic respiration and biochemical oxidation
- Nitrification and denitrification
- The removal of the excess sludge

3. A distributed control solution for the wastewater treatment process: WTP Calafat

3.1. The control architecture

The proposed DCS-SCADA solution for the WTP Calafat is presented in **Figure 3**. The levels of the DCS and their functionality are described in the next paragraphs.

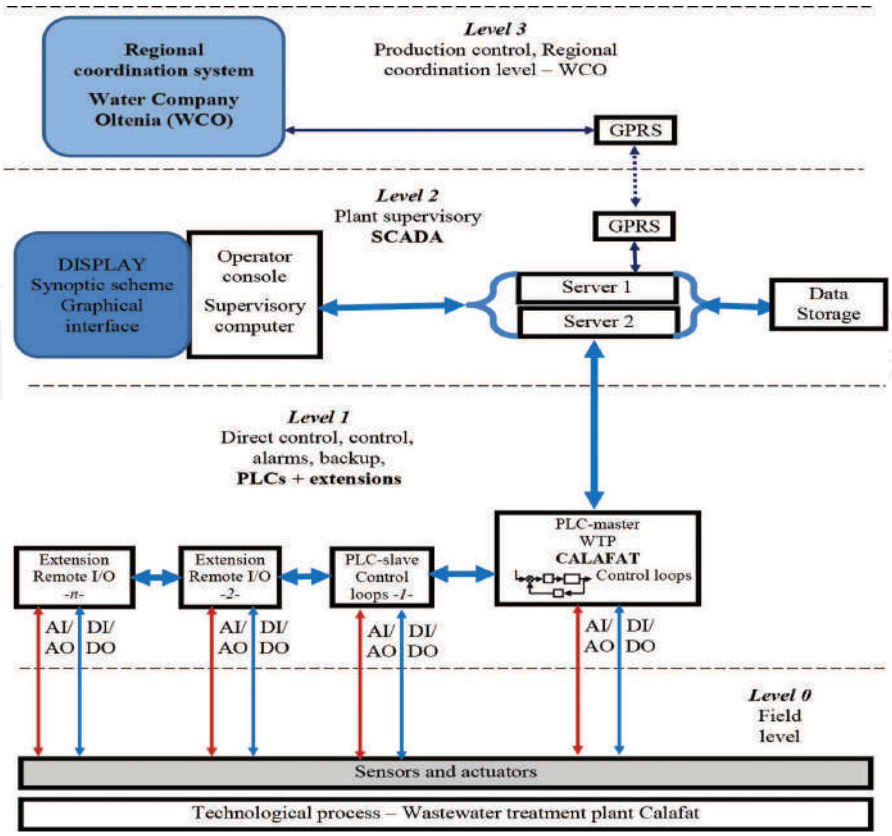

Figure 3. The structure of the DCS with four levels (WTP Calafat).

Level 0 contains all the field devices placed at the technological process level. Classically, at this level we have the measurements of various variables and the final control elements. The components of this level are:

- Sensors (analogic) for flows, levels, pressures, pH, and DO concentrations, such as electromagnetic sensors (Siemens, 0–10 m/s water speed) for flows, ultrasonic sensors (Siemens, 0.3–8 m) for level measurements, pH, and DO concentrations measured via integrated measurement systems (4–20 mA) for dosing devices, etc.
- Contact sensors that provide data about the state of some equipment and operations
- Final control elements (actuators) such as control valves, pumps, etc.
- Dedicated devices for various operations such as dosages, recipes, and technological processing, which will interact with the DCS at the monitoring level
- On/off elements for various actions such as pump starting, etc.

Level 1 comprises the data acquisition devices and the controllers, including the real-time data processing. The analogic signals from sensors and also the control inputs to the actuators are unified signals (e.g., currents in the range 4–20 mA). Due to the geographical distribution, the WTP control system is implemented with several PLCs (programmable logic controllers). These PLCs are connected into a master-slave network with extensions, which handles the information and takes the required decisions for the coordination of the entire technological process. The acquired data, the decisions, and the events occurred in the process are communicated to the next level (SCADA) in order to be used and displayed on the graphical monitoring interface. The information flow is bidirectional; that is, the PLCs receive information about global decisions or optimization, such as set points for the control loops, switches between operational regimes, etc. The decisions at this level are taken in real time and such that the operation of the overall process is managed. The primary control loops are implemented at the PLC level, but the set point of each loop is provided by the superior hierarchic level (SCADA). The PLCs also achieve the implementation of the direct commands delivered by the control algorithms and function of various operational regimes.

Level 2 contains the equipment and the devices from the control room, which receive the information from level 1 (PLC level) and supervise the global operation of the WTP. This level is represented by the SCADA/HMI (human-machine interface) system. The main functions achieved at this level consist in operation optimization, implementation of adaptive and robust control algorithms (proposed in Section 4), operation monitoring via graphical interfaces, remote operation mechanisms, data/event storage, achievement of a data historian, etc. Also, the SCADA ensures the communication between the local dispatcher room (WTP Calafat) and the regional dispatcher of Water Company Oltenia, by using a GSM/GPRS system. The SCADA/HMI runs on two redundant servers. The SCADA supervises the direct control system (real time). If the SCADA system stops, the process will be automatically operated by using the PLCs. Several protection and backup procedures are incorporated in the operation and supervisor programs. The most of control and data acquisition devices used for levels 1 and 2 are provided by Siemens, Telemecanique, etc.

Level 3 is the regional dispatcher of the WCO, and it will coordinate the activity of the WTP with respect of the performance and of extended monitoring of the geographical area.

The operation regimes allowed by the DCS are as follows: automatic, manual via the computer, and locally manual. *Automatic*: The WTP control is achieved exclusively through the command/decision provided by the DCS (PLCs + SCADA/HMI). *Manual via the computer*: The DCS works only as a data acquisition system, but the decisions are taken by the human operator and are transmitted via PLCs and SCADA to the actuators. The system offers all the information and keeps the inter-blockings at the software and hardware levels. This regime can be achieved for the entire WTP or only for some components. *Locally manual*: This regime implies the local operation, no matter what regime is set at the PLCs or SCADA levels. This regime is of high priority, but the SCADA will signalize at the dispatcher level in this situation, and the event will be stored. This regime is useful when failures occur or in the case of network communication problems, startups, and maintenance.

The integration of local SCADA in regional SCADA. The regional SCADA system is a regional centralized structure, which implies the organization of a regional dispatcher, equipped with reliable industrial devices, disposed in a redundant topology in order to ensure a continuous operation. The regional dispatcher role is to coordinate all the subnetworks from the urban areas. The local dispatchers are in fact local process networks from each urban area, which acquire and handle the primary information from the process (levels, flows, concentrations, telemetry, diagnostic signals, etc.). This information is available for the local operator but also at the regional level.

3.2. Level 1: primary control loops

In this section, a few numbers of primary control loops that are implemented at level 1 of DCS-WTP Calafat will be described.

The control loop 1 ensures the level control in the admission room. The level is measured with the sensor L1, and the control action is achieved via the wastewater pumps P1.A, P1.B, and P1.S (two active pumps (A and B) and one for backup (S)). The block diagram of this control loop is presented in **Figure 4**. The level set point is preestablished, since the influent flow in the WTP fluctuates. If the level decreases under a limit, the pumps are shut down (decision at the PLC level). This critical situation is transmitted to the SCADA system, where a warning signal will be displayed/stored. The control loop is a classical feedback loop, with a possible PID control law plus a switching mechanism. The control loop is implemented at level 1 of DCS, but the set point (the reference) is provided by level 2. The actuators are the three pumps P1.A, P1.B, and P1.S that have the motors controlled with static frequency converters in order to provide a variable flow. The switching mechanism (switching logic) of the pumps is designed to ensure a rotation in the operation of the pumps. This fact is done to avoid the unevenly wear of the pumps but also for the failure situations. The influent wastewater flows are disturbances for the loop and will be rejected by the control law.

The control loop 2 is designed for the control of dissolved oxygen (DO) concentrations, which are measured with the transducers Q1 and Q2, and the control is provided by the air blowers A1.A, A1.B, and A1.S. The control loops are presented in **Figure 5** and are dedicated to the DO concentration control in the biological tanks (aerators).

The control laws are PIDs (with self-tuning facilities), but also some advanced control laws can be implemented. As in the previous case, the control loop is implemented at level 1 of DCS, but the set point is provided by level 2. The actuator for the technological line A is the air blower A1.A and for the line B is A1.B (A1.S is a backup air blower).

The control loop 3 is dedicated to the regulation of the recirculated flow percentage calculated from the aerated water flow (from the input of the distribution room). This process variable (percent) is processed by using an algorithm with several input arguments such as dissolved

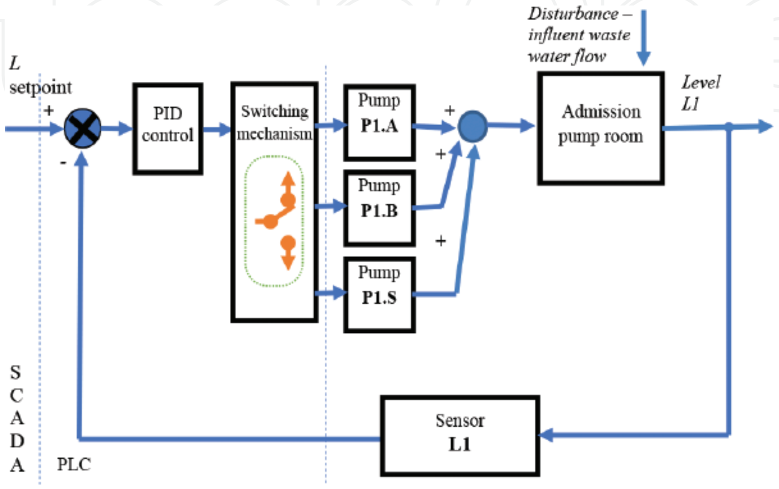

Figure 4. Level control loop: pumps room from the WTP admission.

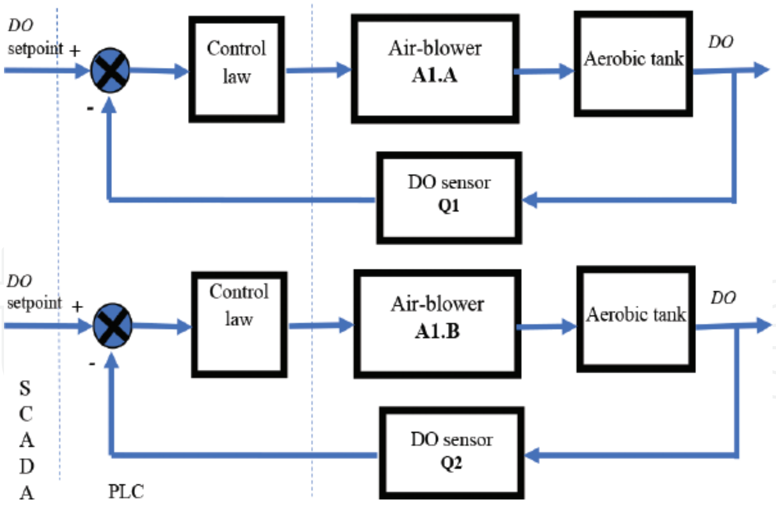

Figure 5. Control loops for the dissolved oxygen concentration.

oxygen, suspended solids, nitrogen, and phosphorus provided by the automated extraction probe system. The set point is given by the operator via the SCADA system, and the control action is based on the emulsion sludge pumps P2.A and P2.B from the aerators. These two control loops (block diagrams in **Figure 6**) are independent because we have two biological treatment tanks. The control loop is implemented at level 1 of DCS, and the set point is provided by level 2. The actuator for the technological line A is the recirculation pump P2.A, and for the line B is the pump P2.B.

The control loop 4 is designed to control the ratio (flow F1)/(flow F2), which is the activated sludge flow introduced in the influent wastewater flow, by using the submersible pumps P3.A, P3.B, and P3.S. This control loop is presented in **Figure 7**. The backup pump P3.S will act:

- Periodically (scheduled by the operator), to ensure a uniform usage of the pumps
- When additional flows of wastewater occur and the active pumps cannot provide the required activated sludge flow
- When some failures occur at the active pumps

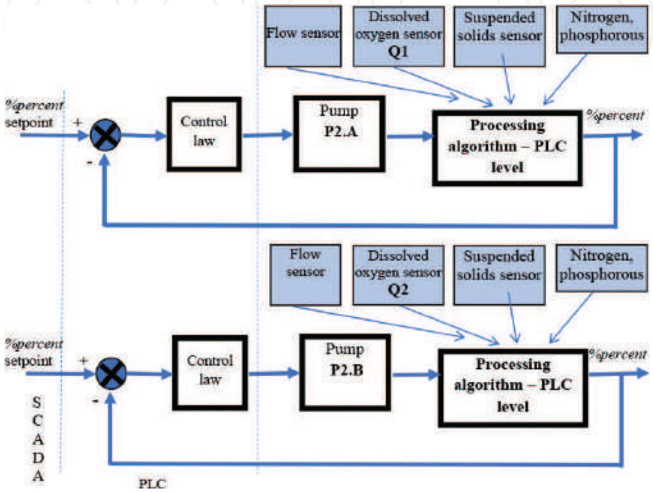

Figure 6. Control loops for the recirculation flows.

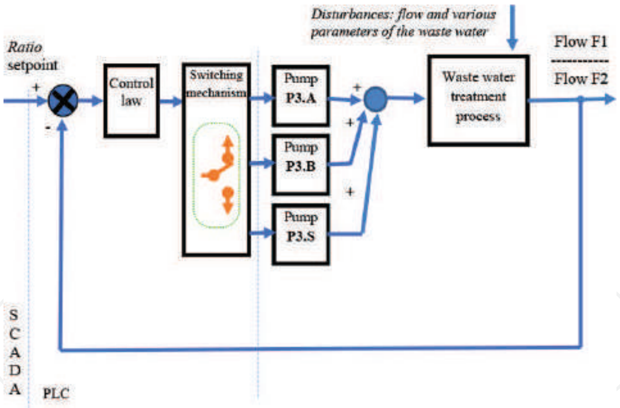

Figure 7. Control loop for the ratio: activated sludge flow/wastewater flow.

As in the previous cases, the control loop is implemented at level 1 of DCS, and the set point is provided by level 2. The actuators are the submersible pumps P3.A, P3.B, and P3.S. The switching mechanism (switching logic) of the pumps is designed in order to cover the above-described scenarios. The influent wastewater flows and their parameters are disturbances for the control loop and will be rejected by the control law.

4. Advanced control solutions for the activated sludge bioprocess

In the following sections, some advanced control solutions are proposed in order to be implemented at level 2 of the DCS-WTP Calafat. More precisely, multivariable adaptive and robust control algorithms are proposed for the activated sludge process that takes place at WTP Calafat. The main control objective at this level is to maintain the pollution level at a desired low value despite the load and concentration variations of the pollutant. The controlled variables are the concentrations of pollutant and dissolved oxygen inside the aerator. Therefore, some of the control loops described in the previous section will be used, and other loops will be modified. The simulations performed in realistic conditions and using an adapted model of the activated sludge process showed that the performance of the overall control system can be increased. The implementation of the proposed control algorithms at WTP Calafat will be ensured within the research project TISIPRO [19].

4.1. Dynamical model of the activated sludge bioprocess and control objective

The activated sludge process which works at WTP Calafat is an aerobic process of biological wastewater treatment. As it was mentioned above, this process is operated in at least two interconnected tanks: a bioreactor (aerator) in which the biodegradation of the pollutants takes place and a sedimentation tank (settler) in which the liquid is clarified (the biomass is separated from the treated wastewater) (**Figure 8**). This bioprocess is very complex, highly nonlinear, and characterized by parametric uncertainties. In the literature there are many models that try to describe the activated sludge processes. The best-known model is ASM1 (Activated Sludge Model No. 1) [3, 10–12]. The main drawback of ASM1 is its complexity, such that it becomes unusable in control issues. Thus, in this chapter a simplified model of a process

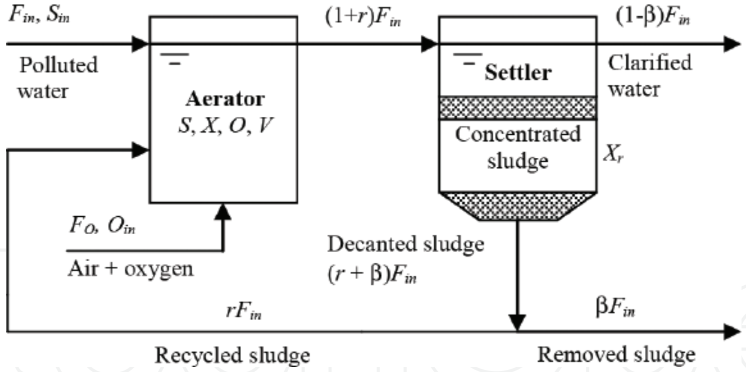

Figure 8. Schematic view of an activated sludge process.

for the removal of the pollutant S from the treated water will be used. The model is based on the model of Nejjari et al. [8], adapted for WTP Calafat. The dynamics of the plant (aerator + settler) is described by the mass balance equations [8, 9]:

$$\begin{aligned}
\dot{X}(t) &= \mu(t)X - \mu_S X - D(1+r)X + rDX_r,\\
\dot{S}(t) &= -(1/Y)\big(\mu(t)X - \mu_S X\big) - D(1+r)S + DS_{in},\\
\dot{O}(t) &= -(K_0/Y)\big(\mu(t)X - \mu_S X\big) - D(1+r)O + \alpha F_O(O_{sat} - O) + DO_{in},\\
\dot{X}_r(t) &= (1+r)DX - \big(r+\beta\big)DX_r,
\end{aligned} \tag{1}$$

where X, S, O, and X_r are the concentrations of biomass (active sludge) in the aerator, of substrate (pollutant), of dissolved oxygen, and of recycled biomass, respectively, O_{sat} is the saturation concentration of dissolved oxygen, $D = F_{in}/V$ is the dilution rate (F_{in} is the influent flow rate, V is the constant aerator volume), μ is the specific growth rate, μ_S is the decay coefficient for biomass, Y is the consumption coefficient of substrate S, r is the rate of recycled sludge, β is the rate of removed sludge, F_O is the aeration rate, and α is the oxygen transfer rate. S_{in} and O_{in} are the substrate and dissolved oxygen concentrations in influent substrate.

If we define $\xi = [X \;\; S \;\; O \;\; X_r]^T$ the state vector of model (1), $\phi = \big(\mu(\cdot) - \mu_S\big)X$ the reaction rate, $v = [0 \quad DS_{in} \quad DO_{in} + \alpha F_O O_{sat}) \quad 0]^T$ the vector of mass inflow rates and gaseous transfer rates, and $K = [1 \quad -1/Y \quad -K_0/Y \quad 0]^T$ the yield vector, then model (1) can be written as

$$\dot{\xi} = K\phi(\xi) - \overline{D}\xi + v \tag{2}$$

where $\overline{D}$ is the matrix of dilution rates, whose structure is the next one:

$$\overline{D} = \begin{bmatrix} D(1+r) & 0 & 0 & -rD \\ 0 & D(1+r) & 0 & 0 \\ 0 & 0 & D(1+r) + \alpha F_O & 0 \\ -D(1+r) & 0 & 0 & D\big(r+\beta\big) \end{bmatrix}. \tag{3}$$

In fact, model (2) describes the dynamics of a large class of bioprocesses carried out in stirred tank reactors and is referred as *general dynamic state-space model* of this class of bioprocesses [3, 7], with $\xi \in \mathfrak{R}^n$, $\phi(\cdot) \in \mathfrak{R}^m$, $K \in \mathfrak{R}^{n \times m}$, $\overline{D} \in \mathfrak{R}^{n \times n}$, and $v \in \mathfrak{R}^n$. The nonlinear character of model (2) is given by the reaction kinetics, its modeling being the most difficult task.

The main *control objective* is to maintain the pollution level at a desired low value despite the load and concentration variations of the pollutant. Because in any aerobic fermentation a proper aeration is essential in order to obtain an efficient process, then an adequate control of dissolved oxygen concentration in aerator is very important [3, 8, 11]. Thus, the *controlled variables* are concentrations of pollutant S and dissolved oxygen O inside the aerator, that is, $y = [S \;\; O]^T$. As *control inputs* we chose the dilution rate D and the aeration rate F_O, that is, $u = [D \;\; F_O]^T$. So, we have a multivariable control problem of a squared process with two inputs and two outputs [12]. Since in model (1) the relative degrees [20] of both controlled variables S and O are equal to one, then the dynamic of output y can be written as

$$\dot{y} = \Psi(\xi) + \Phi^T(\xi)\,\theta + B(\xi)\,u, \tag{4}$$

where $\Psi(\xi)$, $\Phi^T(\xi)$, θ, and $B(\xi)$ are given by.

$$\Psi(\xi) = \begin{bmatrix} (1/Y) \cdot \mu_S X \\ (K_0/Y) \cdot \mu_S X \end{bmatrix}, \Phi^T(\xi) = \begin{bmatrix} -1/Y \\ -K_0/Y \end{bmatrix}, \theta = \mu X, B(\xi) = \begin{bmatrix} S_{in} - (1+r)S & 0 \\ O_{in} - (1+r)O & \alpha(O_{sat} - O) \end{bmatrix} \tag{5}$$

Model (4) is linear with respect to control input $u(t)$.

The matrix $B(\xi)$ is nonsingular and so invertible as long as $S_{in} - (1+r)S$ and $\alpha(O_{sat} - O)$ are different from zero, conditions that are satisfied in a normal operation of the reactor.

We consider that the specific growth rate μ is a double Monod-type model, i.e., [8]

$$\mu(t) = \mu_{\max} \frac{S(t)}{K_S + S(t)} \cdot \frac{O(t)}{K_O + O(t)} \tag{6}$$

where $\mu_{\max}$ is the maximum specific growth rate of microorganisms and K_S and K_O are the saturation constants for substrate S and for oxygen, respectively.

Consequently, based on the input-output model (4), the main *control objective* is to make output y to asymptotically track some desired trajectories denoted $y^* \in \mathfrak{R}^2$ despite any influent pollutant variation and uncertainty and time-varying of some process parameters and also of unavailability of some process states.

4.2. Control strategies

4.2.1. Exact feedback linearizing control

Firstly, we consider the ideal case where maximum prior knowledge concerning the process is available; that is, model (2) is completely known (i.e., μ is assumed completely known and all the state variables, and all the inflow rates are available by online measurements). Then, a *multivariable decoupling exact feedback linearizing control law* can be designed. Since the relative degree of the input-output model (4) is equal to 1, then for the closed loop system, we impose the following first-order linear stable dynamical behavior:

$$(\dot{y}^* - \dot{y}) + \Lambda \cdot (y^* - y) = 0, \tag{7}$$

where $y^* = [S^* \ \ O^*]^T$ is a desired piecewise constant output, $\Lambda = \text{diag}\{\lambda_i\}, \ \ \lambda_i > 0$, and $i = 1, \ \ 2$.

Then, from models (4) and (7), one obtains a *multivariable decoupling feedback linearizing control law*:

$$u = B(\xi)^{-1}\left[\Lambda(y^* - y) - \Psi(\xi) - \Phi^T(\xi)\theta + \dot{y}^*\right]. \tag{8}$$

The control law (8) leads to a linear error model described as $\dot{e} = -\Lambda e$, where $e = y^* - y$ is the tracking error, which for $\lambda_i > 0, \quad i = 1, 2$ has an exponential stable point at $e = 0$.

This controller will be used both for developing of the adaptive and robust controllers and as benchmark, because it yields the best behavior and can be used for comparison.

4.2.2. Adaptive control strategy

Since the prior knowledge concerning the process previously assumed is not realistic, we will design *an adaptive control strategy* under the following conditions:

- The specific growth rate μ is time-varying and completely unknown.
- The variables X and X_r are not accessible.
- The inflow rate F_{in} and the rate of recycled sludge r are time-varying.
- The online available measurements are the output pollution level S; the oxygen concentrations O_{in} and O, respectively; and the influent substrate concentration S_{in}.
- All the other kinetic and process coefficients are known.

Recall that the control objective is to make output y to asymptotically track some specified references $y^* \in \Re^2$ despite the unknown kinetics, any time variation of S_{in}, O_{in}, and F_{in} and time-varying of some process parameters. Under the above conditions, an *adaptive controller* is obtained as follows. The unmeasured variables X and X_r can be estimated by using an appropriate form of the *reaction rate-independent asymptotic observer* developed in [12], described by the next equations (for details, see [12, 15–17]):

$$\dot{\widehat{w}}(t) = W(t)\widehat{w}(t) + Z(t)\zeta_1(t) + Nb(t), \quad \widehat{w}(0) = N\widehat{\xi}(0) \quad \widehat{\zeta}_2(t) = N_2^{-1}(\widehat{w}(t) - N_1\zeta_1(t)) \tag{9}$$

with

$$W(t) = (N_1A_{12}(t) + N_2A_{22}(t))N_2^{-1}, \quad Z(t) = N_1A_{11}(t) + N_2A_{21}(t) - W(t)N_1 \tag{10}$$

This observer was developed for the following class of nonlinear models [12, 15–17]:

$$\dot{\xi}(t) = K\phi(\xi, t) + A(t)\xi(t) + b(t), \tag{11}$$

that can describe the dynamics of numerous bioprocesses, with $x \in \Re^n$, $\phi(\cdot) \in \Re^m$, $K \in \Re^{n\times m}$, $A \in \Re^{n\times n}$, and $b \in \Re^n$. Note that the aerobic process modeled by model (2) belongs to this class.

For a good understanding, we resume here only some aspects. If in model (11) $q \leq n$, states are measured online, and then model (11) can be rewritten as [12, 15–17]:

$$\dot{\zeta}_1(t) = K_1\phi(\xi, t) + A_{11}\zeta_1 + A_{12}\zeta_2 + b_1(t), \quad \dot{\zeta}_2(t) = K_2\phi(\xi, t) + A_{21}\zeta_1 + A_{22}\zeta_2 + b_2(t), \tag{12}$$

where ζ_1 ($\dim\zeta_1 = q$) denotes the measured variables and ζ_2 ($\dim\zeta_2 = n - q = s$) represents the variables that have to be estimated, and the matrices K_1, K_2, A_{11}, A_{12}, A_{21}, A_{22}, b_1, and b_2, with suitable dimensions, are the corresponding partitions of K, A, and b, respectively.

The observers (9) and (10) were developed under the next assumptions about model (11) [12, 15–17]: (H1) K, $A(t)$, and $b(t)$ are known, $\forall t \geq 0$; (H2) $\phi(\xi, t)$ is unknown, $\forall t \geq 0$; (H3) $\operatorname{rank} K_1 = \operatorname{rank} K = p$ with $p \leq m < n$; and (H4) $A(t)$ is bounded, i.e., there exist two constant matrices A^- and A^+ such as $A^- \leq A(t) \leq A^+$ and $\forall t \geq 0$.

The auxiliary variable w ($\dim w = s$) is defined as $w(t) = N\xi(t)$, with $N = [N_1 \vdots N_2] \in \mathfrak{R}^{s\times n}$, where $N_1 \in \mathfrak{R}^{s\times q}$ and $N_2 \in \mathfrak{R}^{s\times s}$ checks the equation $N_1K_1 + N_2K_2 = 0$. If N_2 can be arbitrarily chosen, then $N_1 = -N_2K_2K_1^*$, where K_1^* is a generalized pseudo-inverse of K_1 [15, 21]. Moreover, if N_2 is invertible, then the unmeasured states ζ_2 can be calculated from $w(t) = N_1\zeta_1(t) + N_2\zeta_2(t)$ as $\zeta_2 = N_2^{-1}(w - N_1\zeta_1)$. This condition is satisfied if N_2 is chosen as $N_2 = kI_s$, where $k > 0$ is a real arbitrary parameter and I_s is the s-dimensional unity matrix.

The stability of the observers (9) and (10) can be analyzed by using the observation error $\tilde{\zeta}_2 = \zeta_2 - \widehat{\zeta}_2$, whose dynamics obtained from models (9) and (12) is given by $\dot{\tilde{\zeta}}_2(t) = W_\zeta(t)$ $\tilde{\zeta}_2(t)$, with

$$W_\zeta(t) = N_2^{-1}W(t)N_2 = A_{22}(t) - K_2K_1^*A_{12}(t). \tag{13}$$

It was proven (see [21]) that whatever K_1^* is, the observers (9) and (10) are asymptotically stable if the next conditions hold [15]: (a) $W_{\zeta,ij}(t) \geq 0$ and $\forall i \neq j$, that is, W_ζ is a Metzler matrix [22]; (b) W_ζ^- and W_ζ^+ are Hurwitz stable matrices, with $W_\zeta^\pm(t) = A_{22}^\pm(t) - K_2K_1^*A_{12}^\pm(t)$, where A_{12}^+ and A_{22}^+ and A_{12}^- and A_{22}^- are the corresponding partitions of A^- and A^+, specified in (H4). Since in model (2) $\operatorname{rank} K = 1$, under the above conditions, let us consider the next state partitions:

$$\zeta_1 = [S \;\; O]^T \text{ and } \zeta_2 = [X \;\; X_r \;\;]^T. \tag{14}$$

which are induced on the matrices K, A, and b from model (11) the following partitions:

$$K = \left[K_1^T \vdots K_2^T\right] = [-1/Y \quad -K_0/Y \;\vdots 1 \quad 0]^T, \phi(\xi, t) = \left(\mu(S, O) - \mu_S\right)X,$$

$$A(t) = \begin{bmatrix} A_{11} & \vdots & A_{12} \\ \cdots & \vdots & \cdots \\ A_{21} & \vdots & A_{22} \end{bmatrix} = \begin{bmatrix} -D(1+r) & 0 & \vdots & 0 & 0 \\ 0 & -D(1+r) - \alpha F_O & \vdots & 0 & 0 \\ \cdots\cdots\cdots & \cdots\cdots\cdots\cdots\cdots\cdots\cdots & \vdots & \cdots\cdots\cdots & \cdots\cdots\cdots\cdots\cdots \\ 0 & 0 & \vdots & -D(1+r) & rD \\ 0 & 0 & \vdots & D(1+r) & -D\left(r+\beta\right) \end{bmatrix}, \tag{15}$$

$$b(t) = \left[b_1^T \vdots b_2^T\right]^T = [DS_{in} \;\; \alpha F_O O_{sat} + DO_{in} \;\vdots\; 0 \;\; 0]^T.$$

If the matrix N_2 is chosen as $N_2 = I_2$, then the matrix N_1 from $N = [N_1 \vdots N_2]$ takes the form:

$$N_1 = -N_2 K_2 K_1^* = \frac{1}{(1/Y)^2 + (K_0/Y)^2} \cdot \begin{bmatrix} 1/Y & K_0/Y \\ 0 & 0 \end{bmatrix}. \tag{16}$$

The unmeasured states X and X_r are obtained by using the asymptotic observers (9) and (10) where $W(t)$ and $Z(t)$ are described by the following matrices:

$$W(t) = \begin{bmatrix} -D(1+r) & rD \\ D(1+r) & -D(\beta+r) \end{bmatrix}, \tag{17}$$

$$Z(t) = \frac{1}{(1/Y)^2 + (K_0/Y)^2} \begin{bmatrix} 0 & -(K_0/Y)\alpha F_O(1+r) \\ -(1/Y)D(1+r) & -(K_0/Y)D(\beta+r) \end{bmatrix}. \tag{18}$$

Since $N_2 = I_2$, then $W_\zeta(t) = W(t)$. It is obvious that if $0 < D^- \leq D \leq D^+$ and $0 \leq r^- \leq r \leq r^+$, where D^- and D^+ and r^- and r^+ represent a lower and, respectively, an upper bound of D and r, and $1 \geq \beta \geq 0$, then two stable bounds denoted W_ζ^- and W_ζ^+ can be calculated for the stable matrix $W_\zeta(t)$.

To obtain the online estimates $\widehat{\mu}$ of the unknown rate μ, we will use an observer-based parameter estimator (OBE) (for details, see [3, 7, 21]).

Since for the aerobic digestion we must estimate only one incompletely known reaction rate, using only the dynamics of S and O, then the OBE is particularized as [3, 7, 12]

$$\begin{aligned} \dot{\widehat{S}}(t) &= -(1/Y)(\widehat{\mu} - \mu_S)\widehat{X} - D(1+r)S + DS_{in} + \omega_1\left(S - \widehat{S}\right), \dot{\widehat{O}}(t) = -(K_0/Y)(\widehat{\mu} - \mu_S)\widehat{X} \\ &\quad -D(1+r)O + \alpha F_O(O_{sat} - O) + DO_{in} + \omega_2\left(O - \widehat{O}\right), \dot{\widehat{\mu}}(t) = -(1/Y)\widehat{X} \cdot \gamma_1 \cdot \left(S - \widehat{S}\right) \\ &\quad -(K_0/Y)\widehat{X} \cdot \gamma_2 \cdot \left(O - \widehat{O}\right), \end{aligned} \tag{19}$$

where $\widehat{X}$ is the online estimate of X, calculated by using the state asymptotic observer given in Eqs. (9) and (10), and $\omega_1, \ \omega_2 < 0$ and $\gamma_1, \ \gamma_2 > 0$ are design parameters at the user's disposal to control the stability and the tracking properties of the estimator.

Finally, the complete adaptive control algorithm is made up by combination of the observer Eqs. (9), (10), and (14)–(18) and parameter estimator Eq. (19) with the linearizing control law (8) rewritten as

$$\begin{aligned} \begin{bmatrix} D \\ F_O \end{bmatrix} &= \begin{bmatrix} S_{in} - (1+r)S & 0 \\ O_{in} - (1+r)O & \alpha(O_{sat} - O) \end{bmatrix}^{-1} \left(\begin{bmatrix} \lambda_1 & 0 \\ 0 & \lambda_2 \end{bmatrix} \cdot \begin{bmatrix} S^* - S \\ O^* - O \end{bmatrix} \right. \\ &\quad \left. - \begin{bmatrix} -(1/Y) \cdot (\widehat{\mu} - \mu_S) \cdot \widehat{X} \\ -(K_0/Y) \cdot (\widehat{\mu} - \mu_S) \cdot \widehat{X} \end{bmatrix} + \begin{bmatrix} \dot{S}^* \\ \dot{O}^* \end{bmatrix} \right). \end{aligned} \tag{20}$$

A block diagram of the designed multivariable adaptive system is shown in **Figure 9**.

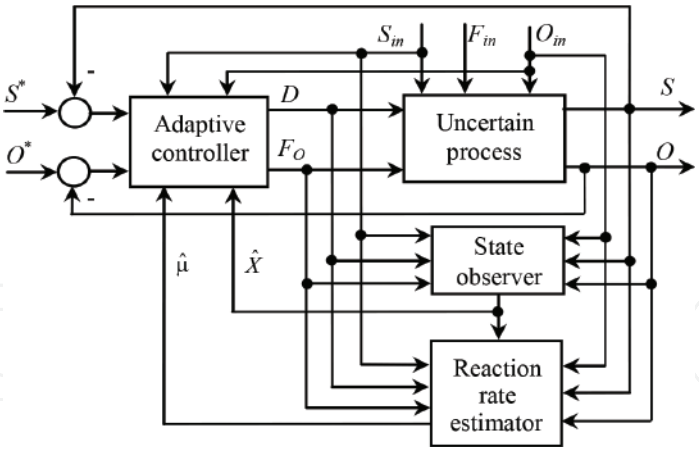

Figure 9. Structure of the adaptive controlled bioprocess.

4.2.3. Robust control strategy

We will develop *a robust control strategy* under realistic conditions as follows:

- S_{in} and O_{in} are not measurable; that is, in model (11) the vector $b(t)$ is incompletely known, but some lower and upper bounds, possible time-varying, denoted by S_{in}^- and S_{in}^+ and O_{in}^- and O_{in}^+, respectively, are given.
- The variables X and X_r are not accessible.
- μ is uncertain and time-varying, because both $\mu_{\max}$ and K_S are uncertain and time-varying, but for these, the bounds $\mu_{\max}^-$ and $\mu_{\max}^+$ and K_S^- and K_S^+, respectively, are known.
- The inflow rate F_{in} is time-varying.
- r is time-varying, but $r \in [r^-, \ r^+]$, where the bounds $r^{\mp}$ are given.
- The available online measurements are S and O.
- All the other kinetic and process coefficients are known.

To control process (1) under the above conditions, we will develop a robust control strategy as follows. First, the components D and F_O of the control law (8) are written as

$$D = \frac{1}{S_{in} - (1+r)S}\left(\lambda_1(S^* - S) + f_D\right), \tag{21}$$

$$F_O = -\frac{O_{in} - (1+r)O}{(S_{in} - (1+r)S) \cdot \alpha(O_{sat} - O)}\left(\lambda_1(S^* - S) + f_D\right) + \frac{1}{\alpha(O_{sat} - O)}\left(\lambda_2(O^* - O) + f_O\right), \tag{22}$$

where

$$f_D = (1/Y)\left(\mu - \mu_S\right)X, f_O = (K_0/Y)\left(\mu - \mu_S\right)X. \tag{23}$$

To estimate the unknown variable X from Eq. (23), we cannot use anymore the asymptotic observers (9) and (10) because S_{in} and O_{in} are not measurable. Hence, by using a suitable *observer interval*, based on the known lower and upper bounds of S_{in} and O_{in}, we estimate lower and upper bounds of X, in-between it evolve. The interval observer is achieved by using the designed asymptotic observers (9) and (10). For this purpose, the hypothesis (H1) is modified into (H1′) as follows: (H1′) K and $A(t)$ are known, $\forall t \geq 0$, and the next additional hypotheses are introduced [15, 16, 21]: (H5) the input vector $b(t)$ is unknown, but guaranteed bounds, possibly time-varying, are given as $b^-(t) \leq b(t) \leq b^+(t)$; and (H6) the initial state conditions are unknown, but guaranteed bounds are given as $\xi^-(0) \leq \xi(0) \leq \xi^+(0)$.

Interval observers work as a bundle of two observers: an upper observer, which produces an upper bound of the state vector, and a lower observer producing a lower bound, providing this way a bounded interval in which the state vector is guaranteed to evolve [15–17, 23]. The design is based on properties of monotone dynamical systems or cooperative systems (see [15–16, 21, 24]). Then, under hypotheses (H1′)-(H6), a robust interval observer for the system (2) can be described as [12, 15–17, 21]

$$(\Sigma^+) = \begin{cases} \dot{w}^+(t) = W(t)w^+(t) + Z(t)\zeta_1(t) + Mv^+(t), \quad w(0)^+ = N\xi(0)^+, \\ \zeta_2^+(t) = N_2^{-1}(w^+(t) - N_1\zeta_1(t)), \end{cases}$$

$$(\Sigma^-) = \begin{cases} \dot{w}^-(t) = W(t)w^-(t) + Z(t)\zeta_1(t) + Mv^-(t), \quad w(0)^- = N\xi(0)^-, \\ \zeta_2^-(t) = N_2^{-1}(w^-(t) - N_1\zeta_1(t)), \end{cases} \tag{24}$$

where $W(t)$ and $Z(t)$ are given by (10), $\zeta_2^+(t)$ and $\zeta_2^-(t)$ are upper and lower bounds of the estimated state $\zeta_2(t)$ and $M = \left[N_1 \vdots |N_{1,ij}| \vdots N_2\right]$, and $v^+(t) = \left[(b_1^+ + b_1^-)/2 \quad (b_1^+ - b_1^-)/2 \quad b_2^+\right]^T$ and $v^-(t) = \left[(b_1^+ + b_1^-)/2 \quad -(b_1^+ - b_1^-)/2 \quad b_2^-\right]^T$, with $b_1^+,\ b_2^+$ and $b_1^-,\ b_2^-$, are the partitions of the known upper and lower bounds of the input vector $b(t)$. Since N_2 must have to be invertible, then it is chosen as $N_2 = kI_s$, where I_s is the identity matrix and $k > 0$ is a real arbitrary parameter.

If the matrix $W_\zeta(t)$ defined in Eq. (13) is cooperative [15–16, 23], then under hypotheses (H1′)–(H6), the pair of systems $(\Sigma^+,\ \Sigma^-)$ constitutes a stable robust interval observer generating trajectories $\zeta_2^+(t)$ and $\zeta_2^-(t)$, and it guarantees that $\zeta_2^-(t) \leq \zeta_2(t) \leq \zeta_2^+(t)$ and $\forall t \geq 0$ as soon as $\xi^-(0) \leq \xi(0) \leq \xi^+(0)$ [15–16, 21]. The convergence of observer (24) can be proven like in [21].

Since the *control objective* is to maintain the wastewater degradation S at a desired low-level S^* with a proper aeration, then under the next realistic conditions $S_{in}^- \leq S_{in} \leq S_{in}^+$, $O_{in}^- \leq O_{in} \leq O_{in}^+$, $\mu_{\max}^- \leq \mu_{\max} \leq \mu_{\max}^+$, $K_S^- \leq K_S \leq K_S^+$, $r^- \leq r \leq r^+$, and $\widehat{X}^- \leq \widehat{X} \leq \widehat{X}^+$ (where $\widehat{X}$ is the estimated value of X, but $\widehat{X}^-$ and $\widehat{X}^+$ are its lower and upper bounds achieved by using the interval observer (24)), we can define the following *robust control strategy*.

If $S < (1 - \varepsilon)S^*$ and $O < (1 - \varepsilon)O^*$, where $0 < \varepsilon \leq 0.05$, represent a dead zone, then***

$$D = \frac{1}{S_{in}^- - (1 + r^+)S}\left(\lambda_1(S^* - S) + f_D^+\right),$$

$$F_O = -\frac{O_{in}^- - (1 + r^+)O}{(S_{in}^+ - (1 + r^-)S) \cdot \alpha(O_{sat} - O)}\left(\lambda_1(S^* - S) + f_D^+\right) + \frac{1}{\alpha(O_{sat} - O)}\left(\lambda_2(O^* - O) + f_O^-\right)$$

else if $(1-\varepsilon)$ and $O>(1+\varepsilon)O^*$, then

$$D=\frac{1}{S_{in}^{-}-(1+r^{+})S}\left(\lambda_1(S^*-S)+f_D^{+}\right),$$

$$F_O=-\frac{O_{in}^{+}-(1+r^{-})O}{\left(S_{in}^{-}-(1+r^{+})S\right)\cdot\alpha(O_{sat}-O)}\left(\lambda_1(S^*-S)+f_D^{-}\right)+\frac{1}{\alpha(O_{sat}-O)}\left(\lambda_2(O^*-O)+f_O^{+}\right)$$

else if $S>(1+\varepsilon)S^*$ and $O<(1-\varepsilon)O^*$, then

$$D=\frac{1}{S_{in}^{+}-(1+r^{-})S}\left(\lambda_1(S^*-S)+f_D^{-}\right), \tag{25}$$

$$F_O=-\frac{O_{in}^{-}-(1+r^{+})O}{\left(S_{in}^{+}-(1+r^{-})S\right)\cdot\alpha(O_{sat}-O)}\left(\lambda_1(S^*-S)+f_D^{+}\right)+\frac{1}{\alpha(O_{sat}-O)}\left(\lambda_2(O^*-O)+f_O^{-}\right)$$

else if $S>(1+\varepsilon)S^*$ and $O>(1+\varepsilon)O^*$, then

$$D=\frac{1}{S_{in}^{+}-(1+r^{-})S}\left(\lambda_1(S^*-S)+f_D^{-}\right),$$

$$F_O=-\frac{O_{in}^{+}-(1+r^{-})O}{\left(S_{in}^{-}-(1+r^{+})S\right)\cdot\alpha(O_{sat}-O)}\left(\lambda_1(S^*-S)+f_D^{-}\right)+\frac{1}{\alpha(O_{sat}-O)}\left(\lambda_2(O^*-O)+f_O^{+}\right),$$

where.

$$f_D^{\pm}=(1/Y^{\mp})\left(\mu^{\pm}-\mu_S\right)\widehat{X}^{\pm},f_O^{\pm}=(K_0/Y^{\mp})\left(\mu^{\pm}-\mu_S\right)\widehat{X}^{\pm} \tag{26}$$

In Eq. (26) the values of μ^+ and μ^- of μ are calculated as $\mu^{\pm}=\mu_{\max}^{\pm}S/\left(K_S^{\mp}+S\right)\cdot O/(K_O+O)$, and $\widehat{X}^-$ and $\widehat{X}^+$ correspond to S_{in}^- and O_{in}^- and S_{in}^+ and O_{in}^+, respectively.

Remark 1. Note that in a normal operation of the bioreactor the terms $S_{in}^{+}-(1+r^{-})S$, $S_{in}^{-}-(1+r^{+})S$, and $\alpha(O_{sat}-O)$ from control law (25) are different from zero.◆

As can be observed from the structure of the control scheme (25) (block diagram in **Figure 10**) and from the simulation results presented in the next section, this control strategy forces the controlled variables to be as close as possible to their desired values.

4.3. Simulation results and discussions

The performance of adaptive controller given by Eq. (20) and of robust controller given by Eqs. (25) and (26) by comparison to the exact linearizing controller (8) (used as benchmark) has been tested by performing extensive simulation experiments. For a proper comparison, the simulations were carried out by using the process model (1) under identical conditions. The values of process and kinetic parameters [8, 12] are adapted for WTP Calafat as in **Table 1**. Two simulation scenarios were taken into consideration:

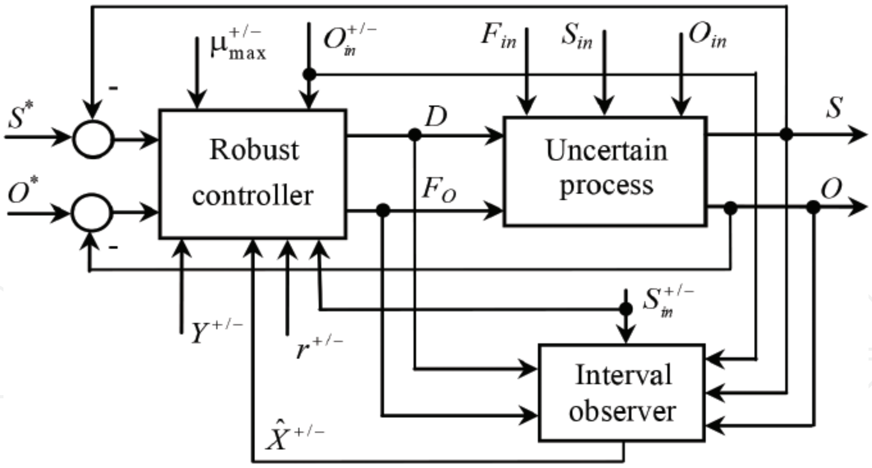

Figure 10. Structure of the multivariable robust controlled system.

Parameter	Value	Parameter	Value
μ_{max}^0	0.15 h^{-1}	α	0.018
K_S^0	100 g/l	β	0.2
K_O	2 mg/l	r^0	0.6
Y	65 g/g	F_{in}^0	6.75 m^3/min
K_0	0.5 mg/g	V	3800 m^3
μ_S	0. 0002 h^{-1}	S_{in}^0	200 mg/l
O_{sat}	10 mg/l	O_{in}^0	0.025 h^{-1}

Table 1. Kinetic and process parameters values.

Case 1. We analyzed the behavior of closed-loop system using the adaptive controller (20), by comparison to exact linearizing control law (8) under the following conditions:

- S_{in} and O_{in} are time-varying (**Figures 11** and **12**), but they are assumed measurable.
- The specific growth rate μ is unknown and time-varying.
- The kinetic coefficients μ_{max}^0 and K_S^0 are time-varying parameters described as $\mu_{max}(t) = \mu_{max}^0 (1 + 0.5\sin(\pi t/10))$, $K_S(t) = K_S^0(1 + 0.25\sin(\pi t/12 + \pi/2))$.
- The rate of recycled sludge r is time-varying as $r(t) = r^0(1 + 0.5\sin(\pi t/36))$.
- The influent flow rate F_{in} is time-varying as $F_{in}(t) = F_{in}^0(1 + 0.2\sin(\pi t/25) + 0.05\sin(\pi t/4))$.
- All the other coefficients (Y, K_O, μ_S, β, α) are constant and known.
- The variables S and O are known (measurable).
- The states X and X_r are unmeasurable (X and X_r will be estimated).

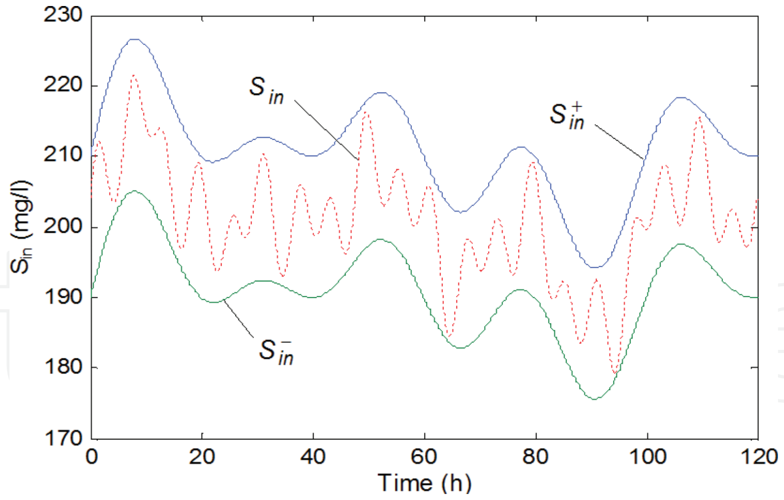

Figure 11. Evolution of S_{in} and of its bounds.

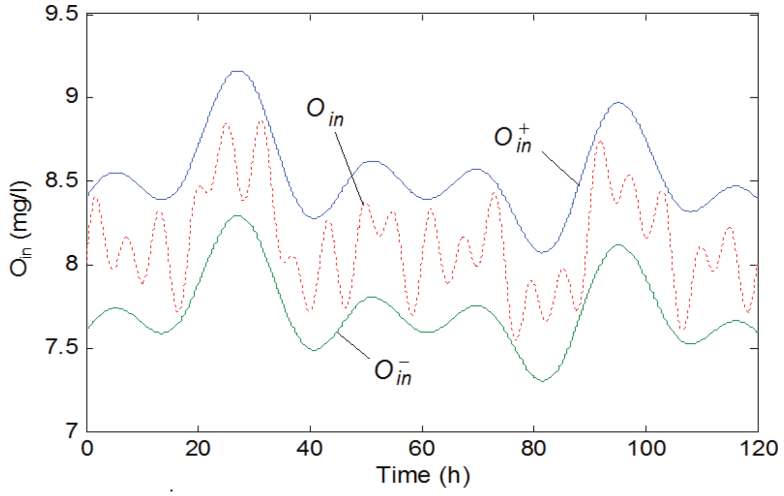

Figure 12. Evolution of O_{in} and of its bounds.

The behavior of closed-loop system using adaptive controller (20), by comparison to exact linearizing control law (8), is presented in **Figures 13–16**. To verify the regulation properties, for references S^* and O^*, some piece-wise constant variations were considered.

To be close to reality, we considered that the measurements of controlled variables S and O are corrupted with additive zero mean white noises (2.5% from their nominal values), as well as the measurements of the influent variables S_{in} and O_{in} are corrupted with an additive zero mean white noise (2.5% from their nominal values). The gains of control laws (8), respectively, (20) are $\lambda_1 = \lambda_2 = 2$, and the tuning parameters of adaptive controller have been set to the values $\omega_1 = \omega_2 = 0.5$ and $\gamma_1 = \gamma_2 = 0.75$.

The evolution of the estimate of unknown variable X provided by the observers (9), (10), and (14)–(18) is presented in **Figure 17**, and the profile of estimate of unknown specific growth rate μ provided by the OBE (19) is given in **Figure 18**. It can be noticed that both state observer and parameter estimator provide proper results. From graphics in **Figures 13** and **14**, it can be seen

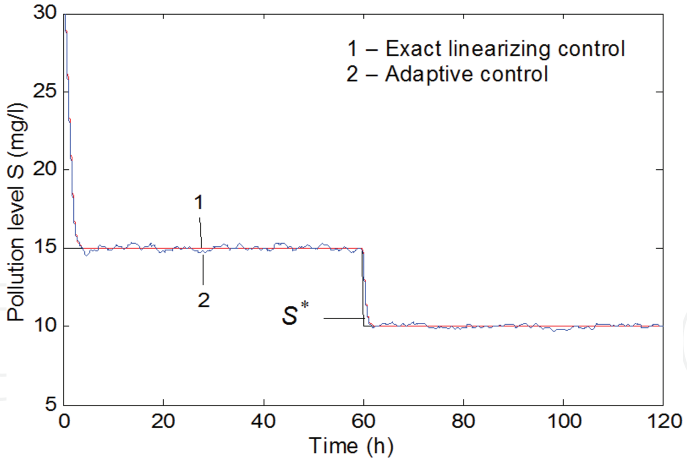

Figure 13. Time evolution of output *S* (Case 1).

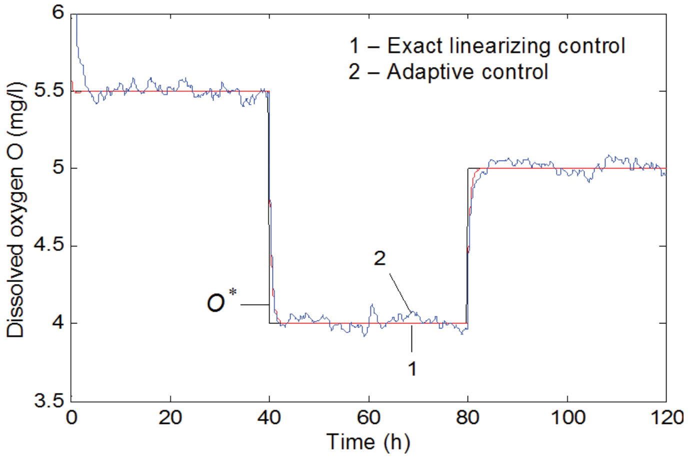

Figure 14. Time evolution of output *O* (Case 1).

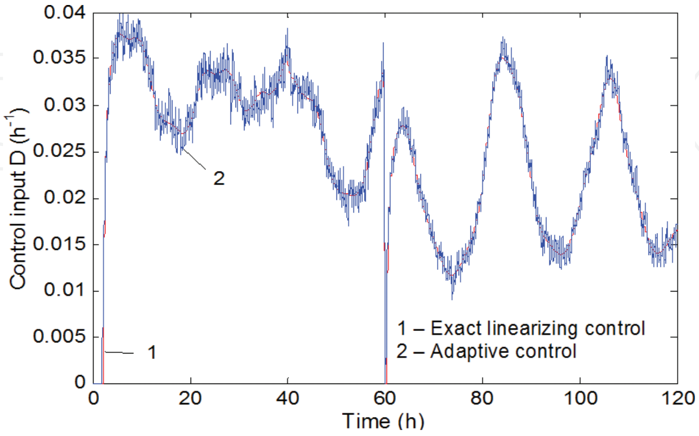

Figure 15. Profile of control input *D* (Case 1).

that the behavior of overall system with adaptive controller (20) is correct, being very close to the behavior of closed-loop system in the ideal case obtained using the linearizing controller (8) when the model is known. Note also the regulation properties and ability of the controller

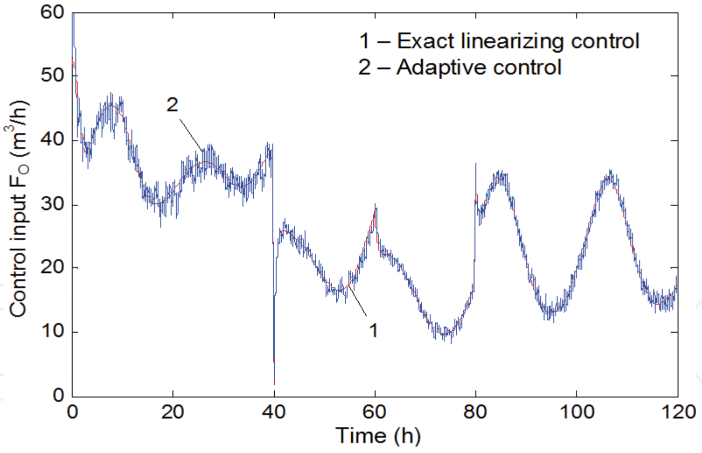

Figure 16. Profile of control input F_O (Case 1).

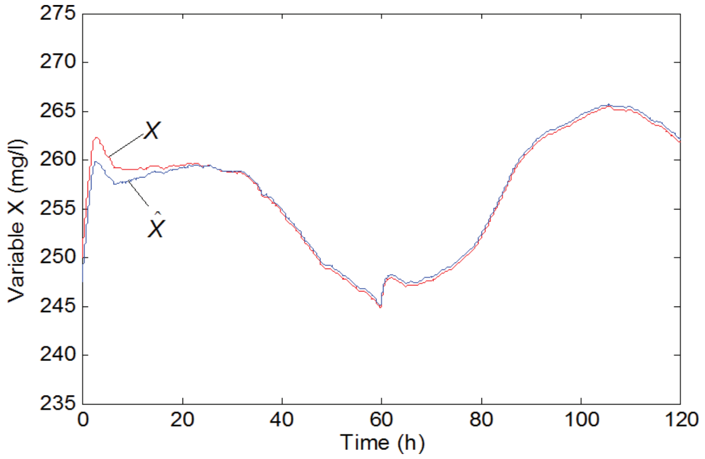

Figure 17. Estimate of unknown X (Case 1).

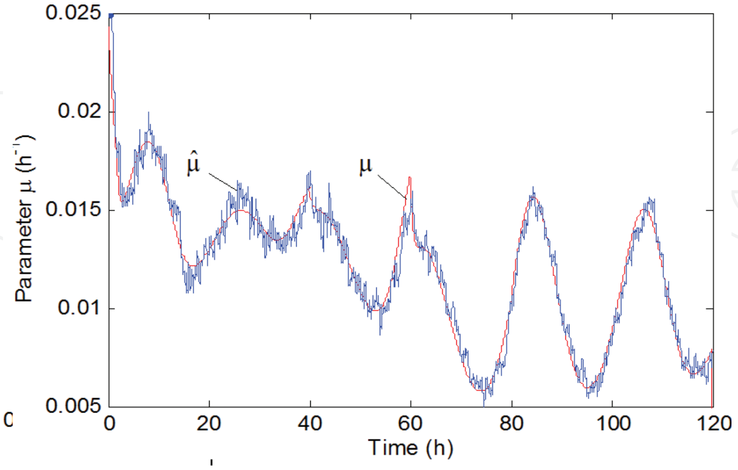

Figure 18. Estimate of unknown rate μ (Case 1).

to maintain the controlled output y very close to its desired value, despite the high variation of S_{in} and F_{in} as well as of the unmeasurable influent dissolved concentration O_{in} and time variation of some process parameters. Even if the control inputs are more affected by noisy measurements, the behavior of the controlled system remains satisfactory.

Case 2. In this case the closed-loop system is based on the structure of robust controllers (25) and (26) under the following assumptions:

- S_{in} and O_{in} are not measurable, but some lower and upper bounds, denoted by S_{in}^- and O_{in}^- and S_{in}^+ and O_{in}^+, respectively, as in **Figures 11** and **12**, are given.
- $\mu_{\max}^0$ and K_S^0 are two uncertain and time-varying parameters, but some lower and upper bounds of them are known, i.e., $\mu_{\max}^- \le \mu_{\max}(t) \le \mu_{\max}^+$ and $K_S^- \le K_S(t) \le K_S^+$.
- F_{in} is time-varying as in Case 1, and the variables S and O are known (measurable).
- The rate of recycled sludge r and the yield coefficient Y are time-varying, but some lower and upper bounds of them are known, i.e., $r^- \le r(t) \le r^+$ and $Y^- \le Y(t) \le Y^+$.
- All the other kinetics and process coefficients are constant and known; states X and X_r are unmeasurable (the lower and upper bounds X^-, X_r^- and X^+, X_r^+ will be estimated, corresponding to S_{in}^- and O_{in}^- and S_{in}^+ and O_{in}^+, respectively).

In our analysis we assume that the time variations of $\mu_{\max}$ and K_S are those from Case 1, that is $\mu_{\max} \in \left[\mu_{\max}^-,\ \mu_{\max}^+\right] = \left[0.5\mu_{\max}^0,\ 1.5\mu_{\max}^0\right]$, and $K_S \in \left[K_S^-,\ K_S^+\right] = \left[0.75K_S^0,\ 1.25K_S^0\right]$.

We assume also that the time variation of r is like in Case 1, that is, $r \in \left[r^-,\ r^+\right] = \left[0.5r^0,\ 1.5r^0\right]$. As we mentioned above, in the control laws (25) and (26), the values of μ^+ and μ^- are calculated as $\mu^\pm = \mu_{\max}^\pm S/\left(K_S^\mp + S\right) \cdot O/(K_O + O)$.

The behavior of closed-loop system using robust controllers (25) and (26) by comparison to the linearizing law (8) is presented in **Figures 19–22**. The gains of control laws (25) are the same as in the first case, i.e., $\lambda_1 = \lambda_2 = 2$. The estimates of lower and upper bounds of variable X are presented in **Figure 23**. The estimated values $\widehat{X}^+$ and $\widehat{X}^-$ are obtained by using the interval observers (24) and (14)–(18), where the input vectors v^+ and v^- contain the known bounds S_{in}^- and O_{in}^- and S_{in}^+ and O_{in}^+, respectively. The state initial conditions are unknown, but some

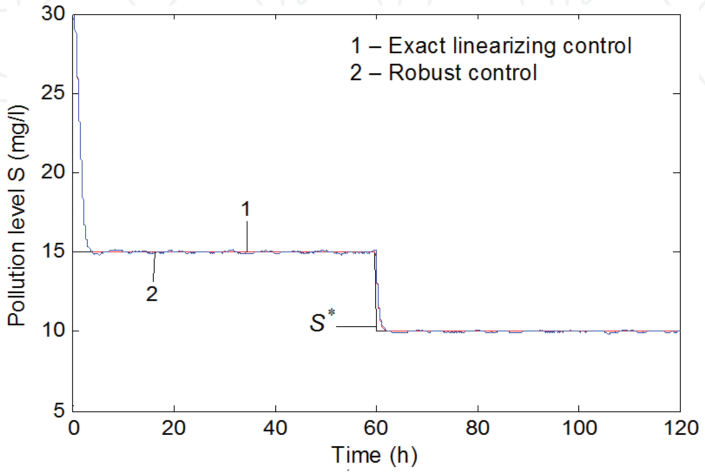

Figure 19. Time evolution of output S—Case 2.

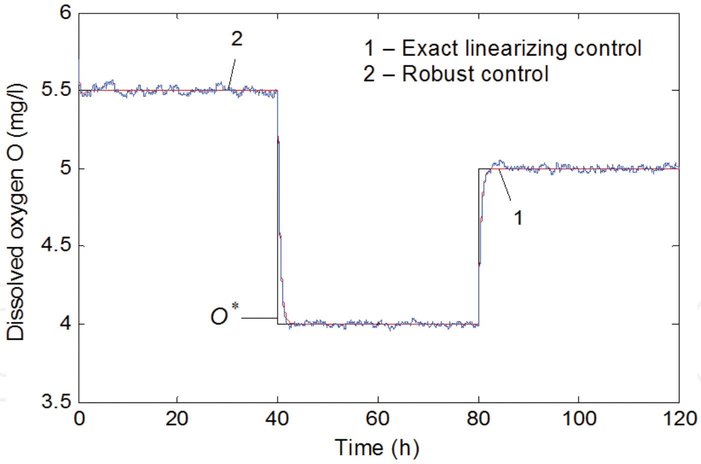

Figure 20. Time evolution of output O—Case 2.

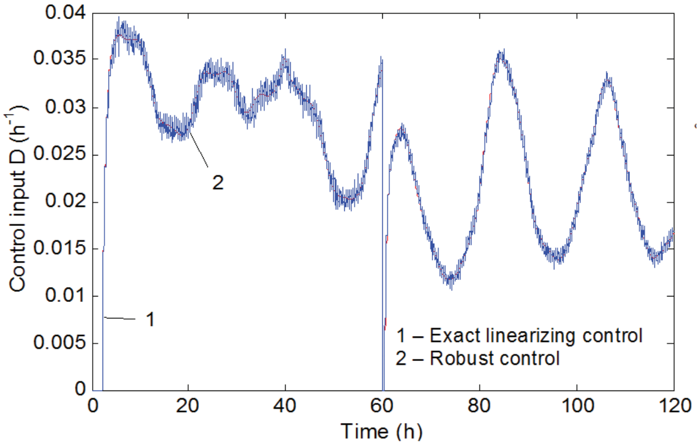

Figure 21. Profile of control input D—Case 2.

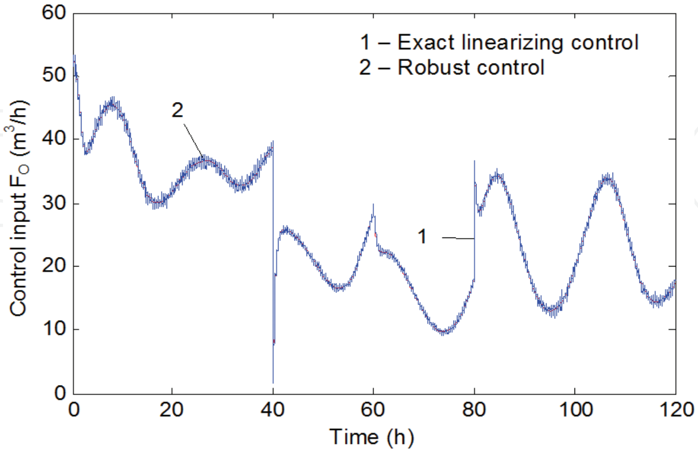

Figure 22. Profile of control input F_O—Case 2.

guaranteed lower and upper bounds are assumed as $245 = X^-(0) \le X(0) \le X^+(0) = 255$ (g/l). The time evolution of the uncertain but bounded time-varying parameter μ as well as of its bounds is shown in **Figure 24**.

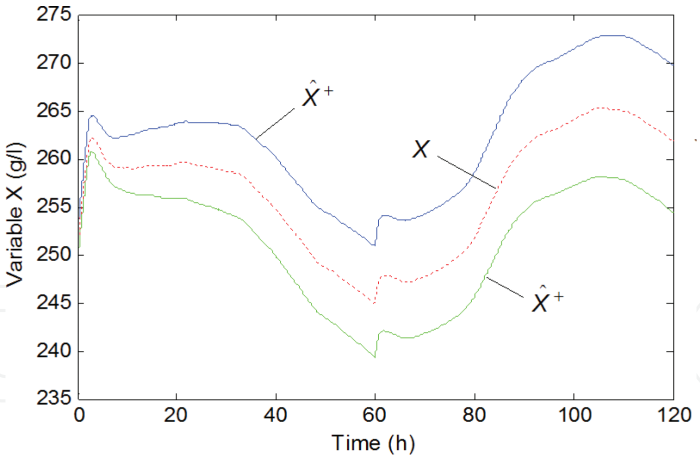

Figure 23. Estimates of bounds of X—Case 2.

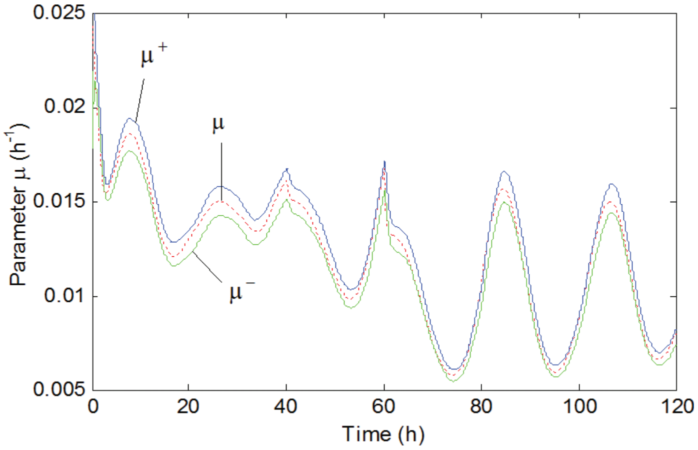

Figure 24. Profiles of μ and its bounds—Case 2.

Note that the reference profiles of S^* and O^* are the same as in the first case. As in the adaptive case, the measurements of controlled variable S and O are corrupted with additive zero mean white noises (2.5% from their nominal values). From **Figures 19–22**, it can be seen that the behavior of overall system with robust controllers (25) and (26), even if this controller uses much less a priori information and is affected by measurement noises, is correct, being close to the behavior of closed-loop system with adaptive controller (20) as well as to the behavior of closed-loop system in the ideal case (process completely known).

5. Conclusions

In this chapter, a distributed and hierarchized control system implemented at WTP Calafat was presented and analyzed. Also, advanced control solutions for the activated sludge bioprocess taking place in the WTP were proposed.

The implemented DCS-SCADA architecture of the WTP was organized as a distributed and hierarchized control system, developed on four levels. The first three levels were approached in this chapter: the field level, the direct control level, and the plant supervisory level. The structure and the functionality of these levels were described. The primary control loops were dedicated to the control of main technological variables such as levels, dissolved oxygen concentrations, recirculation flows, activated sludge flows, etc.

The analysis of the WTP behavior showed that the performance improvement of the control system is possible by developing advanced control solutions for the activated sludge bioprocess that takes place in the WTP. Therefore, multivariable adaptive and robust control algorithms were proposed and will be implemented at level 2 of the DCS.

The main control objective for the activated sludge process is to maintain the pollution level at a desired low value in spite of load and concentration variations of the pollutant. The controlled variables were the concentrations of pollutant and dissolved oxygen. Two nonlinear control strategies were proposed: an adaptive control scheme and a robust control structure. The adaptive control law was developed under the assumption that the growth rates were unknown but the influent flow rate was measurable. The robust control structure was designed under more realistic suppositions that the growth rates are uncertain and the influent concentrations are completely unknown, but lower and upper bounds of growth rates and of influent organic load (possibly time-varying) are known. Also, the uncertain process parameters were replaced by their lower and upper bounds assumed known.

The proposed control strategies were tested in realistic simulation scenarios, by using noisy measurements of the available states. Taking into account all the uncertainties, disturbances, and noisy data acting on the bioprocess, the conclusion is that the adaptive and especially the robust controllers can constitute a good choice for the control of such class of wastewater treatment bioprocesses. As future research, the implementation of the proposed control algorithms for the activated sludge process at WTP Calafat will be ensured within the project TISIPRO. The proposed control architecture and solutions envisaged the WTP Calafat but can be adapted and implemented for other similar WTPs from the WCO.

Acknowledgements

This work was supported by UEFISCDI, project ADCOSBIO no. 211/2014 (2014–2017); by the University of Craiova and Water Company Oltenia, contract no. 168/2017; and by the Competitiveness Operational Program, project TISIPRO no. P_40_416/105736 (2016–2021).

Conflict of interest

The authors declare that there is no conflict of interest about the publication of this chapter.

Author details

Dan Selişteanu, Ion Marian Popescu*, Emil Petre, Monica Roman, Dorin Şendrescu and Bogdan Popa

*Address all correspondence to: pmarian@automation.ucv.ro

Department of Automatic Control and Electronics, University of Craiova, Craiova, Romania

References

[1] ADCOSBIO. Final research report [project report]. Univ. of Craiova—UEFISCDI; 2017

[2] Tchobanoglous G, Burton FL, Stensel HD. Wastewater Engineering: Treatment and Reuse. 4th ed. Metcalf & Eddy, Inc. New York: McGraw-Hill; 2003

[3] Dochain D, Vanrolleghem P. Dynamical Modelling and Estimation in Wastewater Treatment Processes. London: IWA Publishing; 2001

[4] Galloway B, Hancke GP. Introduction to industrial control networks. IEEE Communications Surveys and Tutorials. 2013;**15**(2):860-880

[5] Knapp ED, Langill JT. Industrial Network Security: Securing Critical Infrastructure Networks for Smart Grid, SCADA, and Other Industrial Control Systems. 2nd ed. Waltham: Syngress, Elsevier; 2015

[6] Gupta RA, Chow MY. Networked control system: Overview and research trends. IEEE Transactions on Industrial Electronics. 2010;**57**(7):2527-2535

[7] Bastin G, Dochain D. On-Line Estimation and Adaptive Control of Bioreactors. Amsterdam: Elsevier; 1990

[8] Nejjari F, Dahhou B, Benhammou A, Roux G. Non-linear multivariable adaptive control of an activated sludge waste-water treatment process. International Journal of Adaptive Control and Signal Processing. 1999;**13**(5):347-365

[9] Petre E, Marin C, Selişteanu D. Adaptive control strategies for a class of recycled depollution bioprocesses. Journal of Control Engineering and Applied Informatics. 2005;**7**(2):25-33

[10] Luca L, Barbu M, Caraman S. Modelling and performance analysis of an urban wastewater treatment plant. In: Proceedings of International Conference on System Theory, Control and Computing; 17-19 October 2014; Sinaia. IEEE; 2014. p. 285-290

[11] Henze M, Gujer W, Mino T, van Loosdrecht MCM. Activated Sludge Models ASM1, ASM2, ASM2d and ASM3. IWA Task Group on Benchmarking on Mathematical Modeling for Design and Operation of Biological Wastewater Treatment. London: IWA Publishing; 2000

[12] Petre E, Selişteanu D. A multivariable robust-adaptive control strategy for a recycled wastewater treatment bioprocess. Chemical Engineering Science. 2013;**90**:40-50

[13] Selişteanu D, Petre E, Răsvan V. Sliding mode and adaptive sliding-mode control of a class of nonlinear bioprocesses. International Journal of Adaptive Control and Signal Processing. 2007;**21**(8–9):795-822

[14] Şendrescu D, Popescu D, Petre E, Bobaşu E, Selişteanu D. Nonlinear model predictive control of a lipase production bioprocess. In: Proceedings of International Carpathian Control Conference (ICCC'11); 25-28 May 2011; Velké Karlovice. IEEE; 2011. p. 341-345

[15] Alcaraz-González V, Harmand J, Dochain D, Rapaport A, Steyer JP, Pelayo Ortiz C, González-Alvarez V. A robust asymptotic observer for chemical and biochemical reactors. In: Proceedings of IFAC Symposium on Robust Control Design (ROCOND 2003), 25–27 June 2003; Milan. IFAC; 2003. 6 p

[16] Rapaport A, Dochain D. Interval observers for biochemical processes with uncertain kinetics and inputs. Mathematical Biosciences. 2005;**193**(2):235-253

[17] Alcaraz-González V, Steyer JP, Harmand J, Rapaport A, González-Alvarez V, Pelayo-Ortiz C. Application of a robust interval observer to an anaerobic digestion process. Asia-Pacific Journal of Chemical Engineering. 2005;**13**(3–4):267-278

[18] Selişteanu D, Tebbani S, Roman M, Petre E, Georgeanu V. Microbial production of enzymes: Nonlinear state and kinetic reaction rates estimation. Biochemical Engineering Journal. 2014;**91**:23-36

[19] TISIPRO. Research portfolio no. 4 [project report]. University of Craiova; 2017

[20] Isidori A. Nonlinear Control Systems. 3rd ed. Berlin: Springer-Verlag; 1995

[21] Petre E, Selişteanu D, Şendrescu D. Adaptive and robust-adaptive control strategies for anaerobic wastewater treatment bioprocesses. Chemical Engineering Journal. 2013;**217**: 363-378

[22] Aviles JD, Moreno JA. Cooperative observers for nonlinear systems. In: Proceedings of Joint IEEE Conference on Decision and Control and Chinese Control Conference; 15–18 December 2009; Shanghai: IEEE; 2009. pp. 6125-6130

[23] Moisan M, Bernard O. Interval observers for non monotone systems. Application to bioprocess models. In: Proceedings of IFAC World Congress; 3-8 July 2008; Prague: IFAC; 2008. 6 p

[24] Smith HL. Monotone dynamical systems: An introduction to the theory of competitive and cooperative systems. AMS Mathematical Surveys and Monographs. Vol. 41. Providence, Rhode Island: American Mathematical Society; 1995. 174 pp

Chapter 10

State-of-the-Art Design Technique of a Single-Channel Pump for Wastewater Treatment

Jin-Hyuk Kim and Young-Seok Choi

Additional information is available at the end of the chapter

http://dx.doi.org/10.5772/intechopen.75171

Abstract

A single-channel pump, which is commonly used for wastewater treatment, with a single-channel impeller can effectively prevent performance reduction or damage caused by foreign substances. However, the design methods for this special type of pump are different and more difficult to realize than those for general pumps. In this chapter, a state-of-the-art design technique for a single-channel pump is introduced for realizing high efficiency and low-fluid-induced vibration. In other words, advanced multidisciplinary design optimization techniques combined with unsteady flow analysis are introduced and discussed in detail to simultaneously improve hydraulic efficiency and reduce flow-induced vibration, considering the impeller-volute interaction of a single-channel pump.

Keywords: single-channel pump, wastewater treatment, hydraulic efficiency, flow-induced vibration, radial force, optimization

1. Introduction

The most common fault in a submerged pump is due to waste clogging. This phenomenon causes not only motor overload but also serious damage to a pump system. Hence, this type of pump requires unique design features for preventing losses in performance due to factors such as waste clogging, damage, and failure, unlike general submerged pumps.

Representative types of submerged pumps for wastewater treatment consist of the crushing type and flow-path-securing type. A crushing-type pump mostly crushes and transfers foreign substances with a disintegrator installed in front of the impeller. However, as such types of pumps require the installation of an additional crusher, large-sized solid particles cannot be driven perfectly along the flow path. Moreover, it has a complex structure, high cost, low capacity, and frequent replacement cycle. On the other hand, as a single-channel pump is a representative case of a flow-path-securing type, it has different mechanism features compared with general pumps pressurized by multiblades. A single-channel impeller has one free annulus passage and does not have multiple blades. Further, it is driven by the centrifugal force generated from the rotating annulus passage [1]. Therefore, a single-channel pump is very robust, especially against failure and damage due to waste clogging.

Because of these advantages, the demand for single-channel pumps has increased rapidly in recent times in the field of wastewater treatment. Nevertheless, only a few studies have been published on the design of a single-channel pump [1–4]. To the best of the author's knowledge, the lack of studies can be attributed to the difficulties in establishing a theoretical design methodology, manufacturing, and especially, solving the balancing problem related to the fluid-induced vibration between the impeller and volute of a single-channel pump. In fact, because the mass distribution of a single-channel impeller is not rotationally symmetric, it is difficult to stabilize the fluid-induced vibration between the impeller and volute. Furthermore, unsteady radial forces, which rotate at a frequency generally determined by the rotating speed, are generated in the single-channel impeller [5]. These unsteady sources are generated by the interaction between the rotating impeller and volute, and these adversely affect the overall performance of a single-channel pump, especially its life expectancy and durability.

Over the past several years, there has been growing interest on the effects of unsteady dynamic radial forces due to impeller-volute interaction in centrifugal pumps [6–8]. However, no systematic studies on single-channel pumps have yet been attempted, except for several concepts and patents. To this end, this work presents a state-of-the-art design technique for a single-channel pump for wastewater treatment based on a theoretical approach and three-dimensional steady and unsteady numerical analyses. Moreover, advanced multidisciplinary numerical design optimization techniques are introduced and discussed in detail to simultaneously improve hydraulic efficiency and reduce the flow-induced vibration due to the impeller-volute interaction in a single-channel pump. The objective of this chapter is to provide practical guidelines for optimizing the design of a single-channel pump with the proposed design approach.

2. Basic design approach of single-channel pump

The single-channel pump with an impeller and a volute for wastewater treatment is initially designed according to the Stepanoff theory [9]. The pump can then be modeled as a three-dimensional shape, as shown in **Figure 1** [10]. The three-dimensional model can be developed using commercial modeling software such as SOLIDWORKS and CATIA. Because the Stepanoff theory generally minimizes the flow loss due to flow speed differences by increasing the cross-sectional area of internal flow at a fixed rate according to the theta angle position, it is especially useful for designing a stationary volute. Nonetheless, the impeller of a single-channel pump can be designed based on this concept because it has a free annulus passage

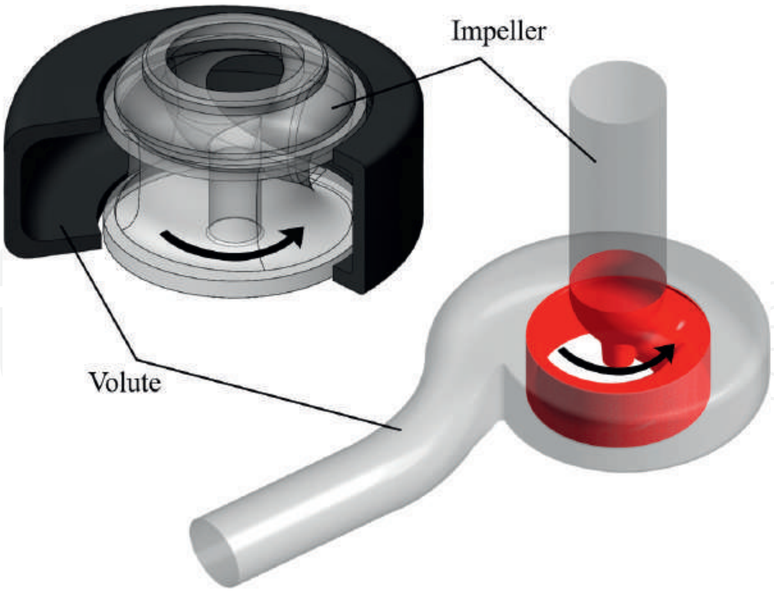

Figure 1. Three-dimensional shape of a single-channel pump [10].

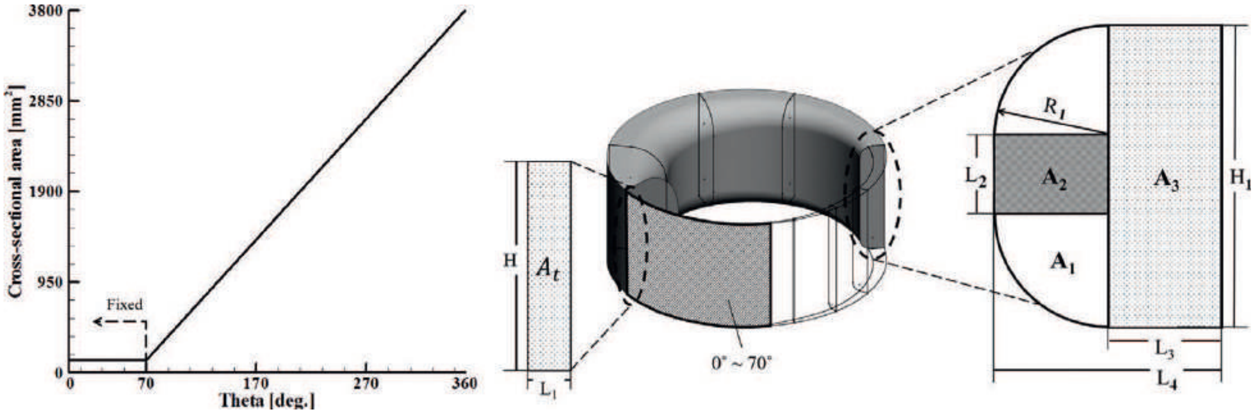

Figure 2. Cross-sectional area distribution and definition of the impeller [10].

and does not contain multiple blades. Further, the impeller is driven by the centrifugal force generated from the rotating annulus passage. Thus, the internal flow distribution in the cross-sectional area of the impeller and volute is changed proportionally with the theta angle position in order to maintain a constant flow velocity. **Figures 2** and **3** show the distribution of internal flows in the cross-sectional area of the impeller and volute generated from the Stepanoff theory. In the authors' previous work, for example, the reference volume flow rate and total head at the design point were 1.42 m^3/min and 10 m, respectively, with a rotational speed of 1760 rpm [11].

When the distribution of internal flows in the cross-sectional area is determined according to the theta angle, the shape of the area should be defined. This shape is very important for deciding the hydraulic performance and size of solid matter in a single channel. In the previous work, the authors proposed a novel design method for defining the cross section of the

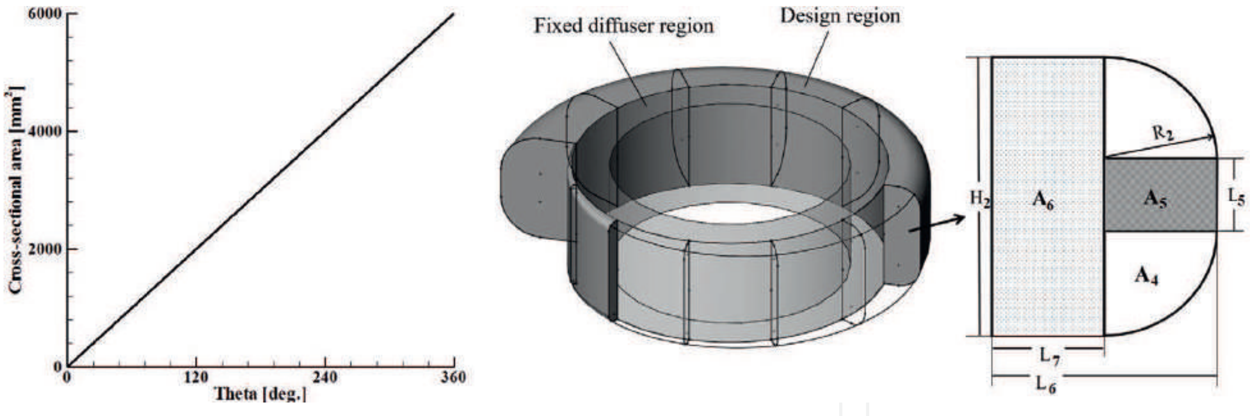

Figure 3. Cross-sectional area distribution and definition of the volute [10].

impeller and volute of a single-channel pump with high performance, as shown in **Figures 2** and **3**, respectively. The cross-sectional area is determined as follows:

The given total area (A_t) in the impeller part,

$$H_1 = 0.835 \times D_1 \tag{1}$$

where the impeller height (H_1) is fixed along theta angle and D_1 represents the inlet diameter of the impeller.

$$A_t\left(@0^\circ \sim 70^\circ\right) = 0.013 \times {D_1}^2 \tag{2}$$

$$L_1 = A_t/H_1 \tag{3}$$

$$A_t\left(@360^\circ\right) = 0.38 \times {D_1}^2 \tag{4}$$

$$A_t = 2A_1 + A_2 + A_3 \tag{5}$$

$$R_1 = \left\{\text{theta}\left(^\circ\right)\text{–}70\ (\text{value of fixed area angle})\right\} \times C_1\ \left(\text{here}, 70^\circ < \text{theta}\left(^\circ\right) \le 360^\circ\right) \tag{6}$$

where $C_1 = 0.1 \times H_1/83.5$ is the expansion coefficient.

$$A_1 = \pi {R_1}^2/4 \tag{7}$$

$$A_2 = R_1 \times L_2 \tag{8}$$

$$A_3 = A_t\text{–}A_2\text{–}2A_1 \tag{9}$$

$$L_3 = A_3/H_1\ (\text{here}, L_3 > 0) \tag{10}$$

The given total area (A_t) in the volute part,

$$H_2 = 0.01 \times A_t\left(@360^\circ\right) \tag{11}$$

where the volute height (H_2) in fixed along theta angle.

$$A_t = 2A_4 + A_5 + A_6 \tag{12}$$

$$R_2 = \text{theta}\left({}^{\circ}\right) \times C_2 \tag{13}$$

where $C_2 = 0.1 \times H_2/89.5$ is the expansion coefficient.

$$A_4 = \pi {R_2}^2/4 \tag{14}$$

$$A_5 = R_2 \times L_5 \tag{15}$$

$$A_6 = A_t – 2A_4 – A_5 \tag{16}$$

$$L_7 = A_6/H_2 \ (\text{here}, L_7 > 0) \tag{17}$$

The cross sections of the impeller and volute are defined as mentioned above. The three-dimensional shape can then be modeled as shown in **Figure 1**. The more detailed explanation can be found in the previous works of the authors [12, 13].

3. Steady and unsteady numerical analyses

In the computation domain generated from the basic design approach, the internal flow field is analyzed by solving three-dimensional steady and unsteady incompressible Reynolds-averaged Navier–Stokes (RANS) equations with a k-ω-based shear stress transport (SST) turbulence model by using a finite volume solver. In this work, the commercial computational fluid dynamics (CFD) code ANSYS CFX 14.5 is used, and ICEM CFD is applied to generate computational meshes for the impeller and volute. The numerical analysis is carried out with boundary conditions, solved, and post-processed using ANSYS CFX-Pre, CFX-Solver, and CFX-Post, respectively.

For the turbulence closure model, the k-ω-based SST model [14] is employed to accurately predict flow separation under an adverse pressure gradient. In this model, the k-ω and k-ε models are applied in the near-wall region and bulk domain, respectively, and a blending function ensures smooth transitions between these two models. The accuracy of the numerical analyses of turbulent flows significantly depends on treating the wall shear stress. In this chapter, the near-wall grid resolution is adjusted to maintain $y+ \leq 2$ to accurately capture the wall shear stress and to implement a low-Reynolds-number SST model.

A tetrahedral grid system is constructed in the computational domain with a prism mesh near the surfaces, as shown in **Figure 4** [15]. The rotating single-channel impeller and the volute domains are each constructed using approximately 1,300,000 and 1,200,000 grid points. Hence, the optimum grid system selected using the grid independency test has approximately 2,500,000 grid points, as previously reported [15, 16].

For the boundary condition, water is considered as the working fluid, and the total pressure and designed mass flow rate are set to the inlet and outlet of the computational domain, respectively. The solid surfaces in the computational domain are considered to be hydraulically smooth under

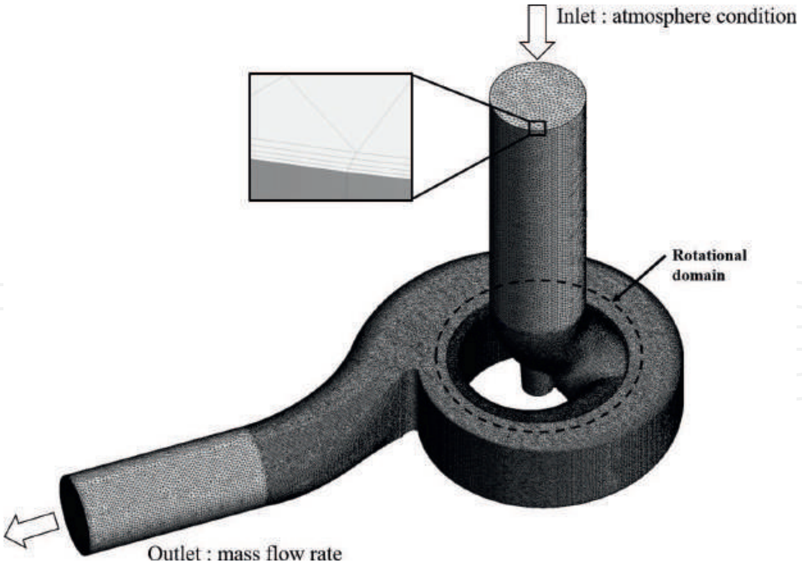

Figure 4. Computational domain and grids.

adiabatic and no-slip conditions. The stage average and transient-rotor-stator methods are respectively applied to connect the interface between the rotating impeller and volute domains in the steady and unsteady analyses.

The convergence criteria in a steady computation consist of the root-mean-square (RMS) values of the residuals of the governing equations, which are set to less than 10^{-5} for all equations. The physical time scale was set to $1/\omega$, where ω is the angular velocity of the impeller. The computations are carried out using an Intel Xeon CPU with a clock speed of 2.70 GHz, and the converged solutions are obtained after 1000 iterations with a computational time of approximately 4 h.

The results of the steady RANS analysis are used in the unsteady RANS analysis to obtain the characteristics of the radial force sources in the region of the exit surface of the impeller according to the impeller-volute interaction in the single-channel pump. In an unsteady simulation, the time step and coefficient loop for the time scale control are set to 0.000947 s and three times, respectively. The solutions are obtained after 180 iterations with an unsteady total time duration of 0.170478 s (five revolutions), and the computational time for the unsteady calculation was approximately 8 h.

4. Optimization techniques

In this chapter, the geometric parameters related to the internal flow through the cross-sectional area of the impeller and volute are selected as design variables to simultaneously optimize the hydraulic efficiency and radial force sources, considering the interaction between the rotating impeller and volute of the single-channel pump. The distribution of internal flow in the cross-sectional area of the impeller and volute can be changed smoothly by adjusting the control points represented by third-order and fourth-order Bezier-curves, respectively, as shown in **Figure 5**. Therefore, the variations in the y-axes for five control points (CP1, CP2, CP3, CP4, and CP5) of both the impeller and volute are selected as design variables to obtain the most sensitive results for the variation in curve among the control points [17].

The aim of the current optimization problem is to simultaneously improve the hydraulic efficiency (η) and reduce the radial force sources considering the impeller-volute interaction in the single-channel pump. Here, one of the three objective functions, that is, the hydraulic efficiency, is defined as follows.

$$\eta = \frac{\rho g H Q}{\tau \omega} \tag{18}$$

where ρ, g, H, Q, τ, and ω denote the density, acceleration of gravity, total head, volume flow arte, torque, and angular velocity, respectively.

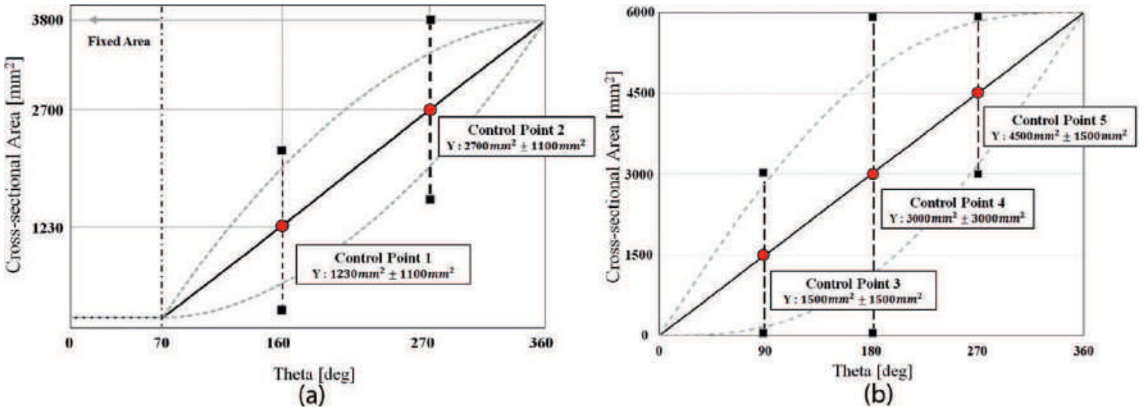

Figure 5. Definition of the design variables. (a) Impeller part (b) Volute part.

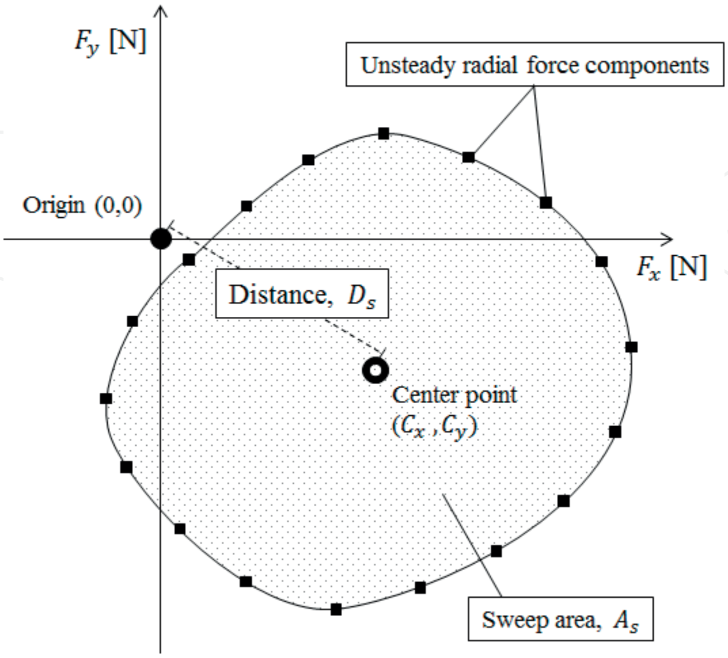

Figure 6. Definition of objective functions related to the radial force sources [10].

The other objective functions related to the radial force sources are defined as the sweep area (As) of the radial force during one revolution of impeller and the distance (Ds) of the mass center of the sweep area from the origin, as shown in **Figure 6**. These functions are defined as follows:

$$A_s = \frac{1}{2}\sum_{i=0}^{n-1}\left(x_i y_{i+1} - x_{i+1} y_i\right) \tag{19}$$

where A_s is the signed area of the polygon as the sweep area of the radial force during one revolution of impeller. The centroid of a non-self-intersecting closed polygon, defined by n vertices (x_0, y_0), (x_1, y_1), …, (x_{n-1}, y_{n-1}), is defined as the point (C_x, C_y) as follows:

$$C_x = \frac{1}{6A_s}\sum_{i=0}^{n-1}\left(x_i + x_{i+1}\right)\left(x_i y_{i+1} - x_{i+1} y_i\right) \tag{20}$$

$$C_y = \frac{1}{6A_s}\sum_{i=0}^{n-1}\left(y_i + y_{i+1}\right)\left(x_i y_{i+1} - x_{i+1} y_i\right) \tag{21}$$

In these formulas, the vertices are assumed to be numbered in the order of their occurrence along the perimeter of the polygon. Therefore, the distance of the mass center of the sweep area from the origin is finally defined as follows:

$$D_s = \sqrt{{C_x}^2 + {C_y}^2} \tag{22}$$

The Latin hypercube sampling (LHS) is employed to generate 54 design points that are used as the initial base data for constructing the response surface from five design variables. LHS, as an effective sampling method for designing and analyzing computer experiments (DACE) [18], is a matrix of order $i \times j$, where i is the number of levels to be examined and j is the number of design variables. Each of the j columns of the matrix containing levels 1, 2, …, i is randomly paired. LHS generates random sample points, ensuring that all portions of the design space are represented. Finally, the objective function values at these design points are evaluated by steady and unsteady numerical analyses.

The response surface approximation (RSA) model is applied as a surrogate model to predict the objective function values based on the 54 design points generated in the design space by using LHS. The RSA model, as a methodology of fitting a polynomial function to discrete responses obtained from numerical calculations, represents the association between the design variables and response functions [19]. The construction function for a second-order polynomial RSA can be expressed as follows:

$$f(x) = \beta_0 + \sum_{j=1}^{N}\beta_j x_j + \sum_{j=1}^{N}\beta_{jj} x_j^2 + \sum\sum_{i \neq j}^{N}\beta_{ij} x_i x_j \tag{23}$$

where β, N, and x represent the regression analysis coefficients, number of design variables, and a set of design variables, respectively, and the number of regression analysis coefficients (β_0, β_i, etc.) is $[(N+1) \times (N+2)]/2$.

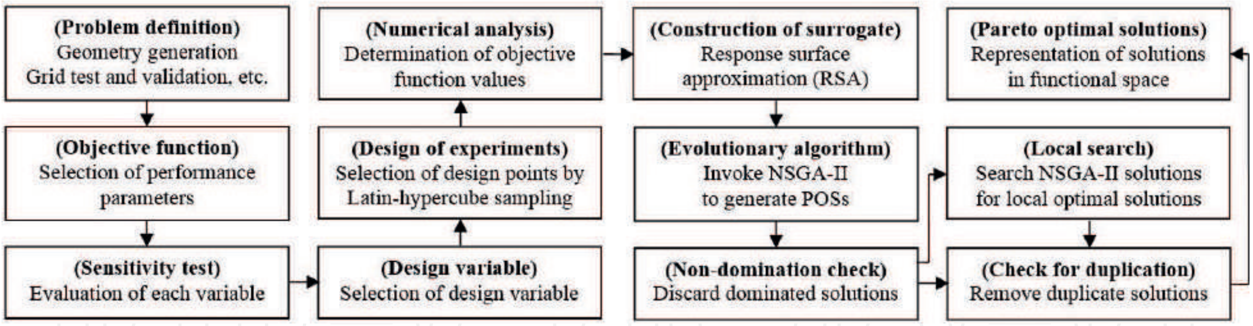

Figure 7. Multiobjective optimization procedure [22].

The RSA models are employed to construct the response surfaces based on the objective function values at the 54 design points generated in the design space using LHS. A hybrid multiobjective genetic algorithm (MOGA) is used to obtain the global Pareto-optimal solutions (POSs). The approximate POSs are obtained using a controlled elitist genetic algorithm (a variant of NSGA-II [20] as the MOGA function for three objective functions. The optimization algorithm and functions in the MATLAB OPTIMIZATION TOOLBOX [21] are used to finally generate the global POSs. **Figure 7** shows an example of the multiobjective optimization procedure [22]. The detailed optimization procedure can be referred to in the previous literatures [23, 24].

5. Results of multiobjective optimization

A hybrid MOGA based on the response surface constructed from the RSA model is employed to obtain the global POSs by using a controlled elitist genetic algorithm (a variant of NSGA-II) for three objective functions. **Figure 8** shows the three-dimensional POSs based on the three objective functions obtained using a hybrid MOGA combined with the RSA model. Here, the values of all the objective function are normalized according to the corresponding values in the reference design. Three-dimensional POSs are obviously the trade-off among the conflicting objective functions. As a result, a trade-off analysis shows an obvious correlation between the hydraulic efficiency and radial force sources. The arbitrary optimum design (AOD) is randomly extracted near the end of the POSs, which exhibits the best performance in terms of all objective functions, as shown in **Figure 8**. The AOD has objective function values that are remarkably improved relative to those in the reference design. Consequently, the value of each objective function in the AOD shows improvements of approximately 49%, 80%, and 4% in the sweep area (As) of the radial force during one revolution, the distance (Ds) of the mass center of the sweep, and the hydraulic efficiency (η), respectively, in comparison with the reference design. On the other hand, a relatively large error among the three objective functions is observed, especially for the distance of the mass center of the sweep. Nevertheless, the values obtained by the numerical analysis are better compared with the reference design.

To understand the optimization results, the trade-off of the POSs in each two-dimensional functional space is shown in **Figure 9**. As shown in **Figure 9(a)** and **(b)**, the decrement in the distance of the mass center of the sweep clearly leads to deterioration in the other objective

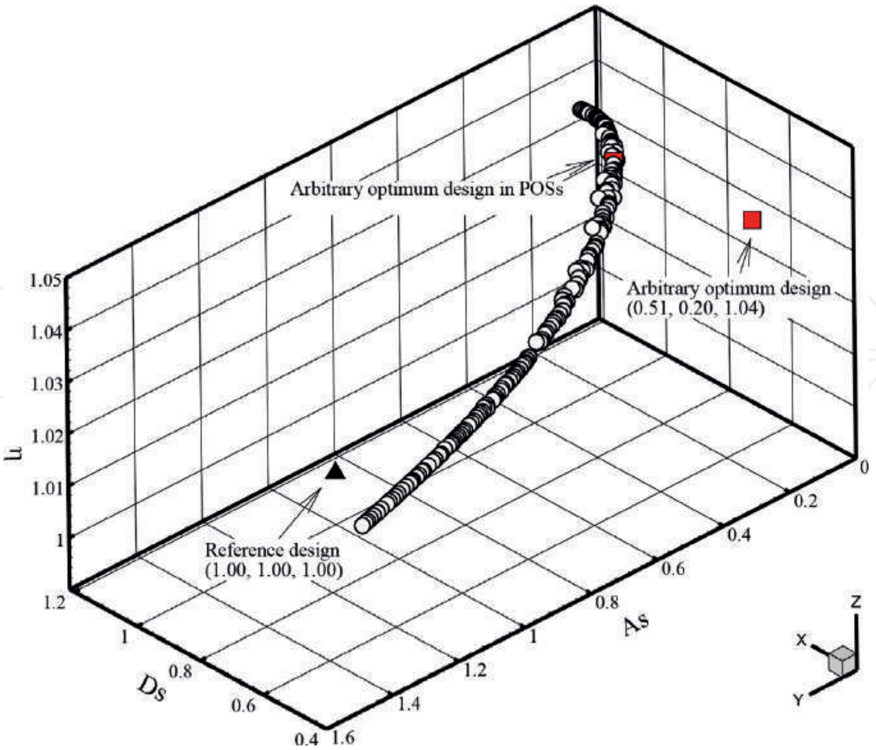

Figure 8. Three-dimensional POSs based on three objective functions. (a) ds-as (b) ds-eff. (c) as-eff.

functions. Specifically, the reduced distance of the mass center of the sweep is obtained at a lower efficiency and higher sweep area of the radial force during one revolution. However, the efficiency and sweep area of the radial force during one revolution shows a positive relation, as shown in **Figure 9(c)**. The trade-off analysis of the POSs therefore allows an engineering designer to choose any economic solution according to the required design conditions.

Figure 10 shows the isosurfaces having a low velocity of 2 m/s. As shown in **Figure 10(a)**, an extremely low-velocity region is formed along the internal wall in the impeller flow path in the reference design, whereas a similar low velocity isosurface is reduced considerably in the arbitrary optimum model (**Figure 10(b)**). These results illustrate the enhancement of hydraulic efficiency in the arbitrary optimum model as a result of optimization.

Figure 11 shows the distributions of unsteady radial force sources, averaged at the boundary surface near the impeller outlet, during one revolution of the impeller for both the reference and AODs. Here, both values are normalized by the value of the maximum radial force in the reference design. The sweep area constructed from the unsteady radial force sources in the reference design leans slightly toward the four quadrant directions from the origin, whereas it is formed near the origin in the AOD. Furthermore, the sweep area in the AOD is remarkably decreased compared with that in the reference design. Consequentially, as discussed already, the sweep area and the distance of the mass center of the sweep in the AOD are decreased by 49% and 80%, respectively, compared with those in the reference design.

Figure 12 shows the unsteady fluctuations of the net radial forces for the reference and AODs during one revolution. Both values are also normalized by the maximum value in the reference

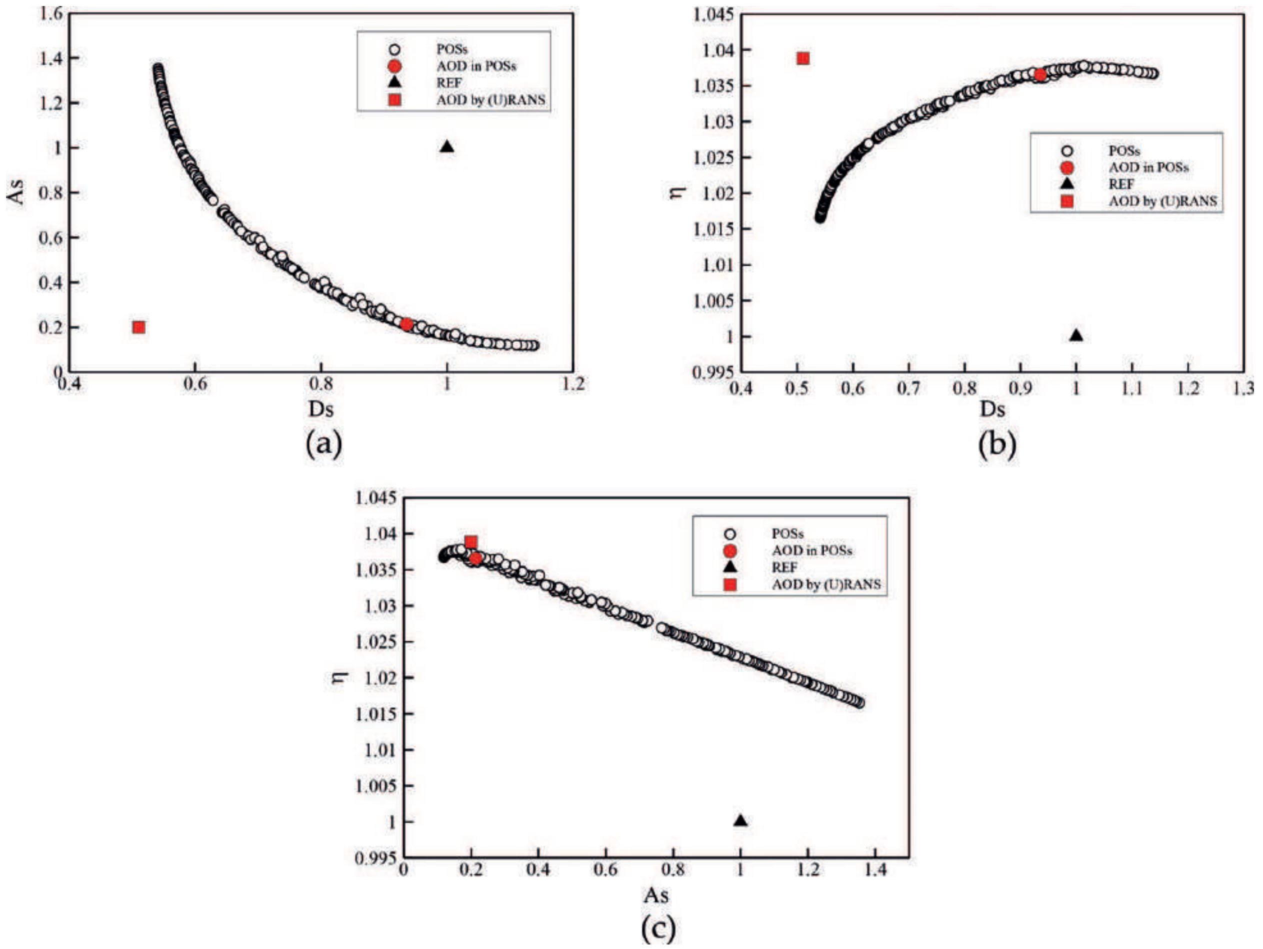

Figure 9. POSs on two-dimensional functional space.

Figure 10. Isosurfaces having a low velocity of 2 m/s. (a) Reference design (b) Arbitrary optimum design.

design. As shown in **Figure 12**, the amplitude values of the fluctuation of the net radial forces in the AOD decrease considerably for most theta angle positions, especially in the region where the value of theta is 100°. In addition, its level is also less than the normalized value of 0.5 and mostly flat compared with the reference design. These phenomena clearly highlight the considerable decrease in the radial force sources as a result of optimization.

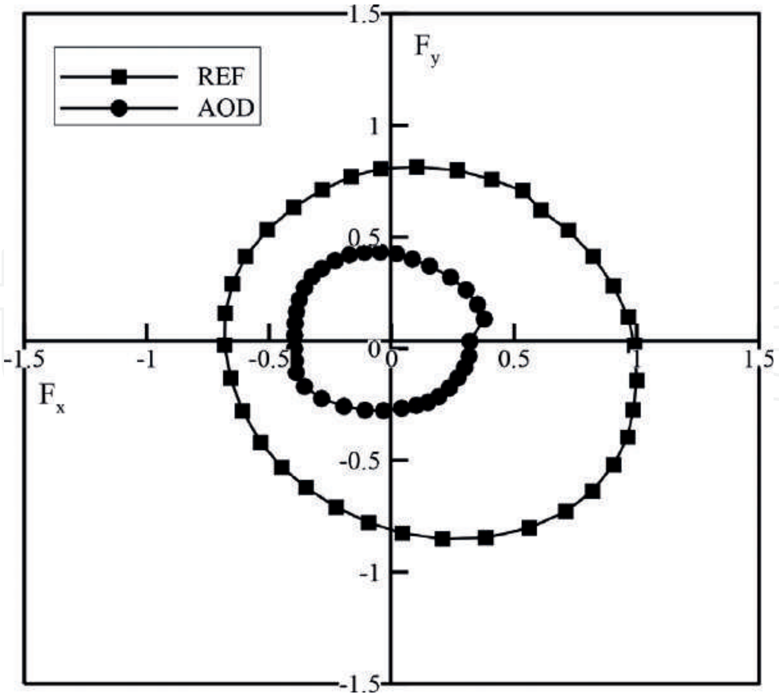

Figure 11. Unsteady radial force distributions during one revolution of the impeller.

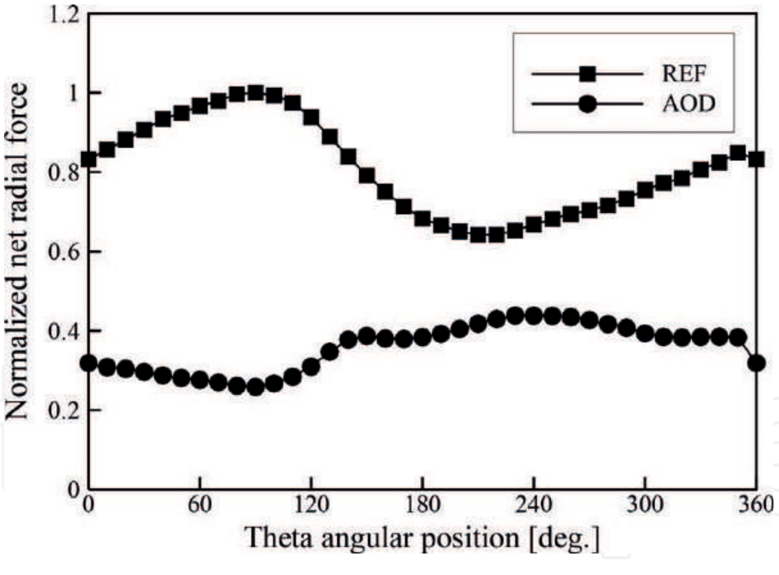

Figure 12. Unsteady net radial force fluctuations during one revolution of the impeller.

Figure 13 shows the time history of instantaneous unsteady pressure contours at the boundary surface near the impeller outlet for both the reference and AODs. Here, both values are normalized by the maximum pressure value in the pressure contours. Both the instantaneous unsteady pressure contours are compared for one rotation τ of the single-channel pump impeller. This rotation is divided into six steps to clarify changes in flow structure with time during one revolution of the impeller, as shown in **Figure 13**. In the reference design, high-pressure zones occur widely on the boundary surface near the impeller outlet, as shown in

(a) $T = 1/6\tau$

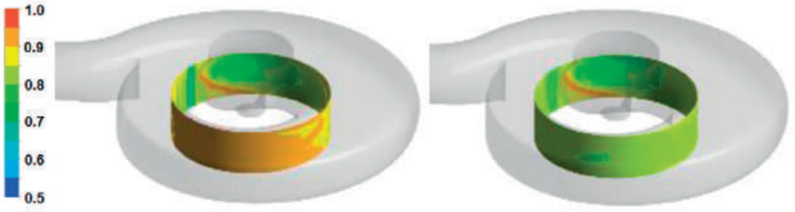

(b) $T = 2/6\tau$

(c) $T = 3/6\tau$

(d) $T = 4/6\tau$

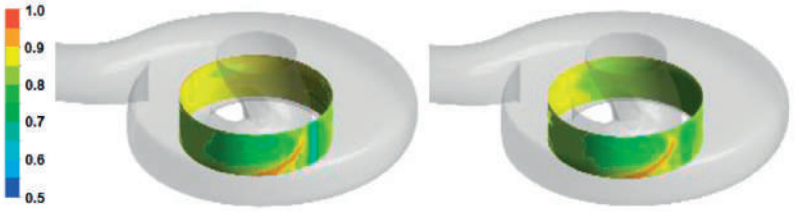

(e) $T = 5/6\tau$

(f) $T = 6/6\tau$

Figure 13. Unsteady pressure contours during one revolution of the impeller. (a) $T = 1/6\tau$. (b) $T = 2/6\tau$. (c) $T = 3/6\tau$. (d) $T = 4/6\tau$. (e) $T = 5/6\tau$. (f) $T = 6/6\tau$.

Figure 13(b), and a high-pressure zone caused by impeller-volute interactions becomes gradually larger. Consequently, this results in the unbalancing phenomena, along with the fluid-induced vibrations caused by unsteady radial forces, throughout the annulus passage area of the pump. Thus, the sweep area constructed from the unsteady radial force sources leans slightly toward the four quadrant directions from the origin, as shown in **Figure 11**. In the AOD, the pressure distribution is generally uniform; especially, at the same instantaneous time, the large high-pressure zone caused by impeller-volute interactions is obviously

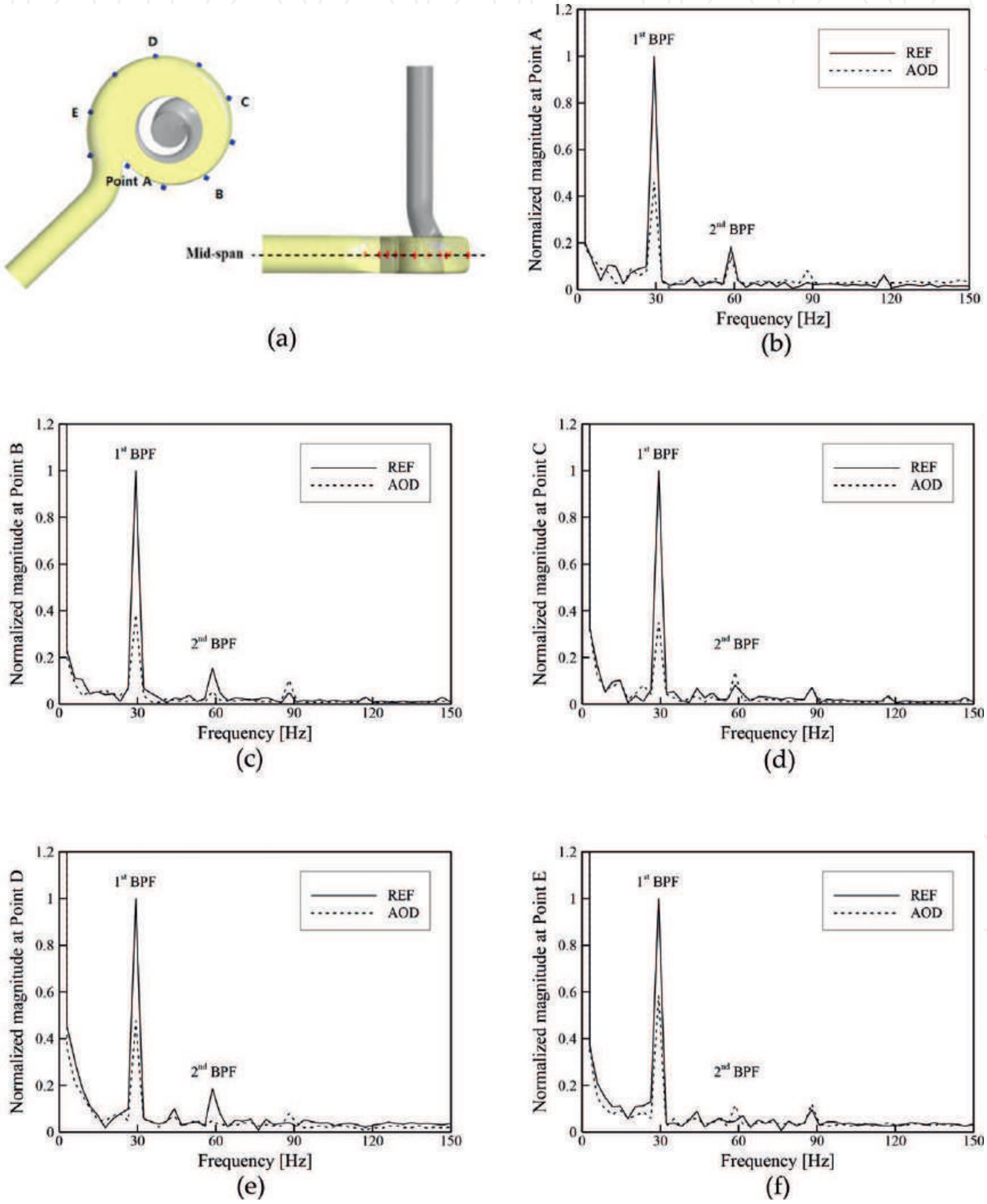

Figure 14. Spectra of the magnitude values at observation points on the casing wall. (a) Location of the observation points (b) Point A. (c) Point B. (d) Point C. (e) Point D. (f) Point E.

suppressed, as shown in **Figure 13(b)**. The AOD results in mostly stable flows throughout the annulus passage area of the pump. This explains the considerable decrease in the fluid-induced vibration caused by impeller-volute interaction owing to optimization.

Figure 14 shows the spectra of the magnitude values at observation points on the casing wall for the reference and AODs. Here, the spectra are calculated based on the wall pressure fluctuation time history by using a fast Fourier transformation algorithm. Both magnitude values are normalized by the first blade passing frequency (BPF) in the reference design, and these values are also related to the vibration of pump. As shown in **Figure 14**, the BPF is approximately 30 Hz (BPF = Blade number × rpm/60). The peak magnitude values are clearly seen at every harmonic BPF in steps of 30 Hz, which are due to the periodic motion of pump impeller rotation. In the AOD, a considerable decrease in the magnitude values at the first BPF is observed specifically, as well as at all observation points, especially for points B and C. It clearly shows that the large high-pressure zone caused by impeller-volute interactions is obviously suppressed, as shown in **Figure 13(b)**. Consequently, the considerable decreases in these magnitude values reduce the vibration caused by impeller-volute interaction.

6. Conclusions

A state-of-the-art design technique was introduced for a single-channel pump for realizing both high efficiency and low-fluid-induced vibration. The technique is based on a theoretical approach and three-dimensional steady and unsteady numerical analyses. Furthermore, advanced multidisciplinary numerical design optimization techniques were discussed in detail to simultaneously improve hydraulic efficiency and reduce the flow-induced vibration caused by impeller-volute interaction in the single-channel pump. The CFD studies conducted in the last decades, along with an increase in computing power systems, have significantly contributed to the development of various turbomachines with a deep understanding of flow physics and mechanism. Of course, it was possible to suggest a state-of-the-art design technique for a single-channel pump because of the rapid increase in the computing power system and development of computational methods. The authors expect that the practical design technique introduced in this chapter will be useful for engineers designing various single-channel pumps in the near future.

Acknowledgements

This work was supported by the Demand-based-Manufacturing Technique Commercialization R&D Project of the Korea Institute of Industrial Technology (KITECH) (No. JB180001), which was funded by the Ministry of Science and ICT (MSIT). The authors wish to express gratefully our thanks to Ms. Bo-Min Cho (former master student in UST and currently CFD engineer in Anflux Co., Ltd., Korea) and Mr. Wang-Gi Song (currently master student in UST) for their cooperation in the numerical simulation.

Conflict of interest

The author(s) declare no potential conflicts of interest with respect to the research, authorship, and/or publication of this article.

Author details

Jin-Hyuk Kim[1,2]* and Young-Seok Choi[1,2]

*Address all correspondence to: jinhyuk@kitech.re.kr

1 Korea Institute of Industrial Technology (KITECH), Cheonan, Republic of Korea

2 University of Science and Technology (UST), Daejeon, Republic of Korea

References

[1] Hansen BF, Henning PJ. Waste water pump. US patent application no. 13. 2013;**886**:479

[2] Zhang H, Chen B, Shi WD, Pan ZY, Cao WD. Effects of contraction-type impeller on non-overloaded performance for low-specific-speed sewage pump. Journal of Mechanical Science and Technology. 2014;**28**(3):937-944

[3] Pei J, Benra FK, Dohmen HJ. Application of different strategies of partitioned fluid–structure interaction simulation for a single-blade pump impeller. Proceedings of the Institution of Mechanical Engineers, Part E: Journal of Process Mechanical Engineering. 2012;**226**(4):297-308

[4] Keays J, Meskell C. A study of the behaviour of a single-bladed waste-water pump. Proceedings of the Institution of Mechanical Engineers, Part E: Journal of Process Mechanical Engineering. 2006;**220**(2):79-87

[5] Gulich JF. Centrifugal pumps. 2nd ed. Berlin: Spring-Verlag; 2008. pp. 548-549

[6] Gonzalez J, Fernandez J, Blanco E, Santolaria C. Numerical simulation of the dynamic effects due to impeller-volute interaction in a centrifugal pump. Transactions of the ASME—Journal of Fluids Engineering. 2002;**124**:348-355

[7] Gonzalez J, Parrondo J, Santolaria C, Blanco E. Steady and unsteady radial forces for a centrifugal pump with impeller to tongue gap variation. Transactions of the ASME—Journal of Fluids Engineering. 2006;**128**:454-462

[8] Baun DO, Köstner L, Flack RD. Effect of relative impeller-to-volute position on hydraulic efficiency and static radial force distribution in a circular volute centrifugal pump. Transactions of the ASME—Journal of Fluids Engineering. 2000;**121**:598-605

[9] Kelder JDH, Dijkers RJH, Van Esch BPM, Kruyt NP. Experimental and theoretical study of the flow in the volute of a low specific-speed pump. Fluid Dynamics Research. 2001;**28**(4):267-280

[10] Cho BM. A study on numerical optimization of flow path cross-sectional area to improve the hydraulic performance of a single-channel pump [thesis]. Daejeon, Republic of Korea, University of Science and Technology; 2017

[11] Kim JH, Cho BM, Kim YS, Choi YS, Kim KY, Kim JH, Cho Y. Optimization of a single-channel pump impeller for wastewater treatment. International Journal of Fluid Machinery and Systems. 2016;**9**(4):370-381

[12] Kim JH, Choi YS, Lee KY, Cho BM. Single channel pump impeller and centrifugal pump having the same. Korea patent application no. 10–2016-0115198. 2016

[13] Kim JH, Choi YS, Lee KY, Cho BM. Single channel pump volute and centrifugal pump having the same. Korea patent registration no. 10–1784561. 2017

[14] Menter FR. Two-equation eddy-viscosity turbulence models for engineering application. AIAA Journal. 1994;**32**(8):1598-1605

[15] Kim JH, Cho BM, Choi YS, Lee KY. Multi-objective optimization based on unsteady analysis considering the efficiency and radial force of a single-channel pump for wastewater treatment. Journal of Mechanics Engineering and Automation. 2016;**6**:234-245

[16] Kim JH, Cho BM, Choi YS, Lee KY, Peck JH, Kim SC. Optimized reduction of unsteady radial forces in a single-channel pump for wastewater treatment. IOP Conf. Series: Earth and Environmental Science. 2016;**49**:032008

[17] Cho BM, Kim JH, Choi YS, Kim JW, Kim YS, Kim KY, Ahn TS, Kim JH. Surrogate based optimization of a single-channel pump impeller. Proceedings of the 7th International Conference on Pumps and Fans 2015 (ICPF 2015); 18–21 October; Hangzhou. China: 2015. ICPF-121

[18] Sacks J, Welch WJ, Mitchell TJ, Wynn HP. Design and analysis of computer experiments. Statistical Science. 1989;**4**(4):409-435

[19] Myers RH, Montgomery DC. Response Surface Methodology: Process and Product Optimization Using Designed Experiments. New York, USA: Wiley; 1995

[20] Deb K. Multi-Objective Optimization Using Evolutionary Algorithms. 1st ed. Chichester, England, UK: John Wiley & Sons Inc; 2001

[21] MATLAB®. The language of technical computing. Release 14. The Math Work Inc; 2004

[22] Kim JH, Kim JW, Kim KY. Axial-flow ventilation fan design through multi-objective optimization to enhance aerodynamic performance. Transactions of the ASME—Journal of Fluids Engineering. 2011;**133**:101101

[23] Afzal A, Kim KY. Three-objective optimization of a staggered herringbone micromixer. Sensors and Actuators B: Chemical. 2014;**192**:350-360

[24] Shim HS, Afzal A, Kim KY, Jeong HS. Three-objective optimization of a centrifugal pump with double volute to minimize radial thrust at off-design conditions. Proceedings of the Institution of Mechanical Engineers, Part A: Journal of Power and Energy. 2016;**230**(6): 598-615

Sustainable Sorbent Materials Obtained from Orange Peel as an Alternative for Water Treatment

Irma Robles Gutierrez, Ana K. Tovar and
Luis A. Godínez

Additional information is available at the end of the chapter

http://dx.doi.org/10.5772/intechopen.76137

Abstract

The presence of pollutants in water promotes negative impacts on aquatic organisms. Among the methods of wastewater treatment, the use of sorbent materials is one of the most outstanding due to its efficiencies and easy implementation. Orange peels had become value-added products for these purposes. Activated carbon as a sorbent material was prepared using orange peel as a precursor. The resulting material was physicochemically characterized by scanning electron microscope (SEM) and Fourier transform infrared radiation (FTIR); structural changes were identified and related to sorption capacity using a model pollutant. Results of sorption indicated natural dried orange peel which presented a sorption capacity of 149.26 mg/g, while sorbent-activated carbon presented a sorption capacity of 2342.91 mg/g. The recovery of orange peel to obtain potential interest materials provided benefits for wastewater treatment.

Keywords: orange peel, sorbent material, activated carbon, valorization, wastewater treatment

1. Introduction

The industry of agricultural products processing, or agribusiness, is defined as the economic activity that combines the agricultural productive process with the industrial processing to obtain food or semi-processed raw materials. Among the industrialized products are fruits, vegetables, seeds, tubers and pods; some are marketed fresh and others are transformed into nectars, juices, jams, flours, oils, and wines, among others.

After the processing of these products, agroindustrial waste is obtained. Agroindustrial waste is solid or liquid materials generated from the direct consumption of primary products or its industrialization. Those residues are no longer useful for the process that generated them, but they are susceptible to transformation to obtain another product with economic value, of commercial and social interest [1].

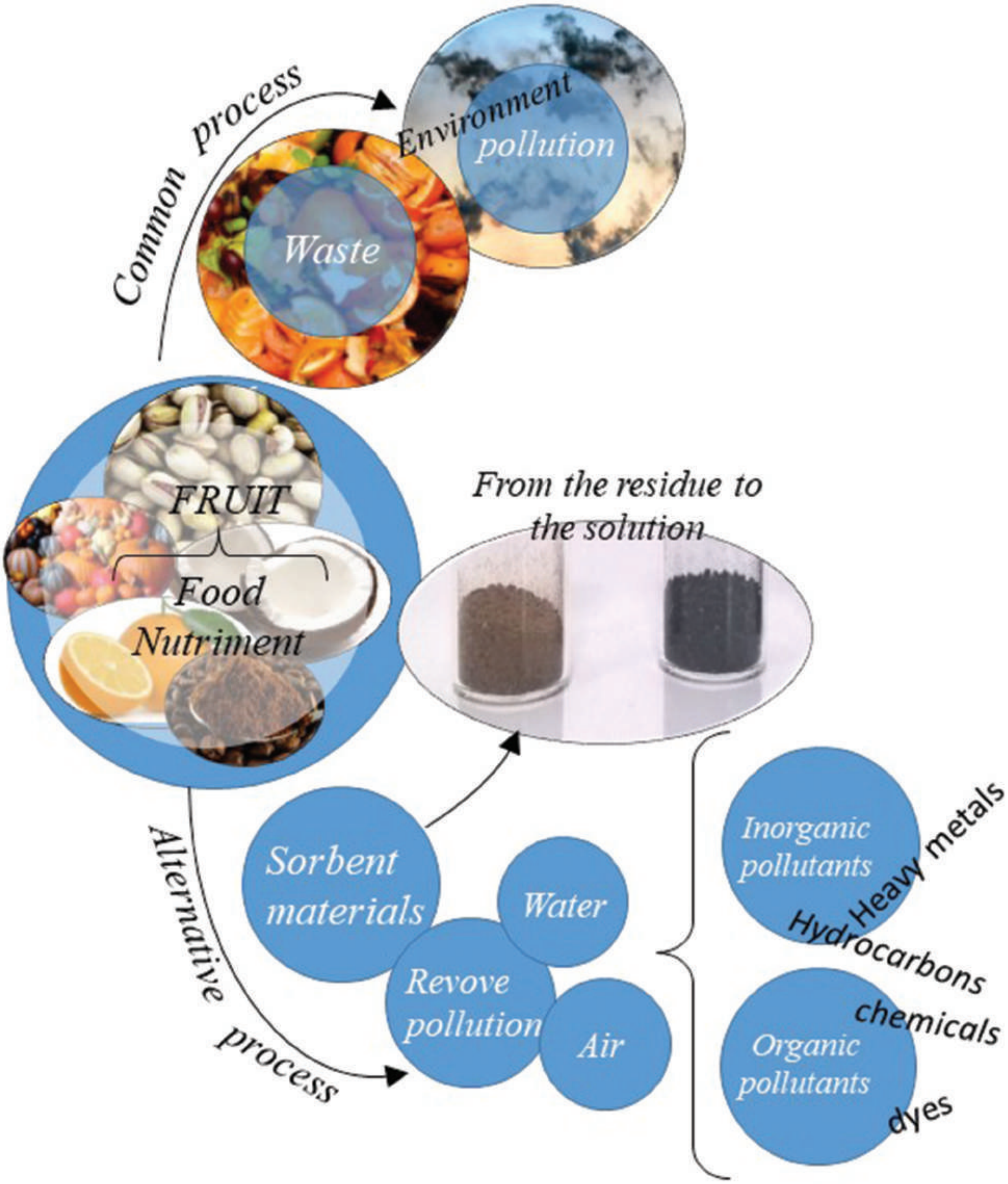

Figure 1. Alternatives for organic residue waste management.

The food industry is characterized by a considerable generation of waste and byproducts. Despite the environmental repercussions that this represents, the amount of agroindustrial waste has increased continuously. Orange peels represent a clear example of agroindustrial waste, which is the result of fruit processing for the production of juices. Due to the large volume of generation and the environmental risk they represent, some investigations have focused on the valorization of this waste through extraction of value-added products or even transformation to other materials.

Valorization of waste is an attractive approach that offers potentially useful alternatives to treat waste, instead of disposal or landfill deposition. In general, agroindustrial waste possesses varied characteristics, which depend on the raw material and the process that generated those residues; however, they share a similar characteristic, that is the organic matter content, constituted by different percentages of cellulose, lignin, hemicellulose, and pectin. The valorization of food waste components could give numerous possibilities for obtaining value-added products [2]. **Figure 1** represents different alternatives for organic residue waste management, on the one hand, the common use of waste that implies it's wasted, and even its contribution to the environment and, on the other hand, some possibilities to use them as materials for environment protection from the use of sorbent materials.

2. Orange fruit

In the orange Mexican harvest, the volume of production has averaged 4.3 million tons in the last 6 years. The national market is the main trade of Mexican orange; an average of 67.53% of the supply of fresh oranges is destined for national production; most of them are designated to homes, restaurants, street vendors, and hotel chains, among others [3, 4].

Since orange has a high production in the country, as well as in the world, and serves as the main raw material for agroindustrial processing, the amount of fruit marketed to the juicing industry has increased [3].

The orange processing industry accommodates a small percentage of 32% in the last years [4]. Since 2004, the percentage of fruit destined to the juice agroindustry increased significantly due to government programs which allowed the recovery of the freight and collection costs of the fruit marketed to the Mexican agroindustry of oranges (**Table 1**). Simple juice and concentrated juice are the main products in the processing of citrus fruits [3].

Production	2011	2012	2013	2014	2015	2016
Mexico	83	151	126	159	165	170
EUA	681	607	476	438	383	355
Brazil	1263	980	1230	1006	848	1222

Table 1. Main producing countries of orange juice, considering 1000 metric tons at 65° BRIX.

The oranges processed in the industry are destined in its majority to the juice export market (**Table 2**). Studies show that Mexico, in comparison with large producing countries, has been increasing the amount of juice produced over the years. Mexico has had a great inclusion in the international market, satisfying the demand of countries such as the United States, Canada, and Japan, among others [3, 4].

Production	**2011**	**2012**	**2013**	**2014**	**2015**	**2016**
Mexico	2011	2012	2013	2014	2015	2016
EUA	79	143	121	153	158	163
Brazil	110	114	113	81	66	65

Table 2. Export data of orange juice, considering 1000 metric tons at 65° BRIX.

3. Orange peels

Orange peels are waste generated mainly by the juicing industry that can cause environmental problems due to its large volume of generation and physicochemical characteristics, such as soil and water pollution. For this reason, the recovery and transformation of orange peels has become a topic of interest for recent investigations; one important alternative is the preparation of sorbent materials.

The waste material of the orange industry is constituted mainly by peels, shells, seeds, and capillary membranes. When leaving the industry, the orange peels have a high level of organic matter and low pH; such indicators demonstrate the potential polluting. Since the composition of orange peels can be transformed to use as raw material for the production of national interest products, in this way, value-added products can be obtained due to the valorization process, and, at the same time, it is possible to reduce the environmental impact [5, 6].

3.1. Physicochemical composition of orange peel

The chemical composition of orange peels, shown in **Table 3**, makes them an attractive source of industrial products. Soluble sugars present in orange peels are composed mostly of sucrose, glucose, and fructose, while organic acids are composed of citric, oxalic, and succinic acid. The fiber is the portion of the shell where the pectin is contained. The pectins contained in the orange fiber are soluble and insoluble in the form of protopectin [5].

However, resent investigations of citrus waste focus on the recovery of a single component, such as d-limonene, pectin, or bioethanol [8].

Recent investigations have shown that orange peel is a potentially valuable resource that can be transformed into value-added products; the most common alternatives have reported the use of this material as livestock feed, source of heat generation, biomethanization, and compost [9, 10].

Parameter	Value
Soluble solids (°Brix)	7.10 ± 1.2
pH	3.93 ± 0.003
Acidity[1]	0.29 ± 0.003
Formaldehyde	34.00 ± 2.4
Moisture (%)	60.5
Ash (%)[2]	3.29 ± 0.19
Fat content (%)[2]	0.2
Protein (%)[2]	1.5
Carbohydrates (%)[2]	89.00 ± 1.1
Pectin (%)[2]	170.00 ± 5
Lignin	3.20 ± 0.4
Essential oils (mL/kg)	1.45 ± 0.16

[1] g of citric acid/100 mL.
[2] db = dry basis.

Table 3. Physicochemical composition of the orange peel [7].

4. Sorbent materials obtained from orange peels

The elaboration of high-quality sorbent materials from agroindustrial waste opens an effective path for the conversion of these residues into high value added products [11].

Activated carbons are commonly used as sorbent materials due to their sorption capacity; those activated carbons are produced from a wide variety of carbon-based materials. Those materials used for the production of activated carbon are carbon-based organic materials, such as coal, lignite, and wood. Although natural coal is the most used precursor, agroindustrial waste is considered as a good alternative; in this way, the activated carbon produced from waste would reduce the demand of forests since wood is also used for this purpose [12].

According to International Union of Pure and Applied Chemistry (IUPAC), an activated carbon is a porous carbonaceous material that has been subjected to gas reaction, sometimes with chemical agents, during or after carbonization process in order to increase its sorption properties.

The use of carbon-based materials goes so far back in history, since charred wood and mineral coal or simply partially volatilized coal materials were already used for similar purposes.

From 1901, several patented methods of activated carbon production were registered. In this way, R. Von Ostrejko patented two methods to produce activated carbon: one based on the carbonization of lignocellulosic materials with metal chlorides (the basis of chemical activation) and the second method based on a gentle gasification of coals with water vapor or carbon dioxide (basis of physical activation) [13].

Nowadays the activated carbons are prepared from a carbon precursor such as lignite, wood, or synthetic precursors, mainly of polymeric type such as resins.

A typical carbonization process produces around 20–30% carbonization yield, where the activating agent is a dehydrating compound, which would increase the amount of active sites, favored by the thermal degradation of the precursor, modifying in this way the porosity of the obtained material. Precursors such as lignocellulosic materials reflect the botanical texture of the precursor [14].

Many of the laboratory uses and industrial applications of activated carbons are based on the high sorption capacity of the material. This capacity depends on the physical properties of the coal, as well as its chemical structure [15].

4.1. Chemical structure of activated carbons

The structure of the activated carbon is considered as a continuous descent in the degree of ordering of the planes in the graphite. However, activated carbon also has a three-dimensional structure of carbon atoms in flat sheets of hexagonal rings. However, unlike graphite, there is no crystallographic order in the third dimension, and the cross-linking of the plates can occur [13].

The spaces between the graphite planes of crystals create the microporous structure, with a high internal surface area [16]. According to IUPAC, pores of activated carbons can be classified into micropores (pore diameter <2 nm), mesoporous (pore diameter between 2 and 50 nm), and macropores (pore diameter >50 nm) [13].

In addition to the porous structure, activated carbons have a chemical structure, since they contain small amounts of heteroatoms. The presence of heteroatoms (O, N, H, S, etc.) attached to the edges of the graphene layers gives rise to a variety of surface functional groups [16], which allow polar substances to be weakly retained on the surface of activated carbon. This is because the carbon atoms located at the edges of the planes have a high available activity, since they are not saturated with carbon atoms and have free electrons [13].

Oxygenated functionalities are the most important due to their surface properties and can also be developed spontaneously through the exposure of the material to the inert atmosphere. Chemisorbed oxygen can only be removed from the surface as CO or CO_2 at temperatures above 120°C. The unsaturated carbon atoms at the edges of the basal crystal planes are associated with high concentrations of mismatched electrons, which play a very important role in the chemisorption process [16].

Oxygenated functional groups are not formed exclusively by the reaction with oxygen; these groups can also be the results of the reaction with other oxidizing gases (O_3, N_2O, CO_2) and oxidizing solutions (HNO_3, H_2O_2). In addition, the electron density π of the basal carbon planes is considered as chemically active [16]. The surface chemistry of activated carbon has an amphoteric nature due to the coexistence of acidic and basic surface groups. An activated carbon is globally acidic or basic depending on the surface concentration of these groups and also on the strength of acidic or basic compounds [13]. Therefore, the oxygenated surface groups are classified into the categories mentioned in the following sections.

4.1.1. Basic surface groups

These groups are formed when the oxidized surface is reduced by an inert or hydrogen atmosphere, at high temperatures. The decomposition of acidic groups creates active sites at the edges of graphene plates, which can attract oxygen during the cooling stage in an inert atmosphere, and after a process of reexposure to air, forming basic functional groups such as chromene and pirona.

4.1.2. Acidic surface groups

These groups are formed when the carbon surface is exposed to oxygen through reactions with oxidizing agents in solutions or the gas phase; this process can be carried out at room temperature or even at high temperatures, these parameters are responsible for the amphoteric characteristic of the activated carbons, which depend on the pH of the aqueous phase.

4.1.3. Hydrogenated groups

Hydrogen atoms are usually present in the surface of activated carbons such as chemisorbed water, as part of other surface groups such as carboxylic acids, phenols, amines, or even directly attached to carbon atoms as part of aromatic or aliphatic structures.

4.1.4. Phosphorus groups

Phosphorus atoms contained in activated carbons generally come from the phosphoric acid used as an activating agent in the preparation stage. Once phosphorus is located in the carbon matrix, it can be stable between 500 and 1000°C; this atom can be found as red phosphorus or chemically bonded as —C—P— or —C—O—P—. Phosphorus-containing species can be formed during carbonization at low temperature ranges [16].

4.1.5. Activated carbon preparation

The physicochemical properties of each activated carbon depend mainly on the source of the starting material, since it essentially determines the structural characteristics of the resulting material [14].

Through the carbonization process, it is possible to obtain a low surface area, as elements such as oxygen and hydrogen are eliminated by decomposition of the starting material in an inert atmosphere, usually nitrogen. The resulting material is formed by unions of elementary graphitic microcrystals, usually plugged by tars and carbonization residues, which notably decrease the sorption capacity. In order to increase the sorption capacity of this coal, it will be necessary to resort to some method that allows eliminating tars, by means of some oxidizing agent as the activating agent [14]. There are two activation processes, called physical activation and chemical activation, described below [13].

4.1.6. Physical activation

This method consists of an oxidation step that is usually carried out in the presence of water vapor, carbon dioxide, or air; the activation treatment is carried out at high temperatures

(>700°C) [15]. These agents are capable of extracting carbon atoms from the porous carbon structure according to the following stoichiometry equations; these equations describe the endothermic reactions. This method of activation is known as physical or thermal activation [14].

$$C + CO_2 \rightarrow 2CO \tag{1}$$

$$C + H_2O \rightarrow CO + H_2 \tag{2}$$

In this process, two differentiated stages can be considered: a first one, in which all the disorganized materials are burned, and a second one, in which the pores that were initially closed or blocked are opened. As a result of that, a new material with a high surface is produced, due to the presence of large porosity [17].

4.1.7. Chemical activation

Chemical activation involves the carbonization of the precursor in the presence of an alkali, hydroxides (KOH, NaOH), or inorganic acids (H_3PO_4, HNO_3, H_2SO_4) [16].

The yield of activated carbon prepared by chemical activation method is usually higher than those activated carbons prepared under physical activations. In order to compare physical and chemical methods, it is possible to emphasize that, while in the physical activation method, the development of pores is mainly promoted by the removal of carbon atoms by a gasification process; in the chemical activation method, the activation agents promote dehydrogenation reactions in the precursor that promote bonds' formation between carbon atoms and also the creation of pores on the surface.

Unlike physical activation, the preparation of activated carbons by chemical activations is carried out in a single stage; the carbonization and activation process are carried out simultaneously. Chemical activation requires lower carbonization temperatures than physical activation. In addition, chemical activation leads to a better formation of the porous structure.

As a result of the carbonization and activation processes, activated carbons with porous characteristics are obtained which are determined by various factors such as starting material (precursor), size of the precursor particles, activating agent, activation temperature, heating rate, temperature and carbonization time, etc. [12, 16].

4.2. Sorption on solid surfaces

The forces that hold a solid bonded to the surface of activated carbons produce a field force around each ion, atom, or molecule. At the surface of the solid, these forces cannot suddenly disappear, and due to these unsaturated and unbalanced forces, the solid has the tendency to attract and retain on its surface molecules and ions of other substances with which it is in contact. Thus, when the surface of the solid is in contact with a gas or a liquid, the concentration of the gas or liquid is always greater in the surface of the solid than in the interior of the gas or liquid phase. The substance adhered to the surface is called sorbate, and the material in which it is sorbed is called sorbent. Depending on the nature of the forces involved, the sorption process is classified into two main types [18]:

4.2.1. Physical sorption

The sorbate is bounded to the surface of the activated carbon by relatively weak Van der Waals forces, identical to the molecular forces of cohesion that are involved in the condensation of vapor on liquids.

4.2.2. Chemical sorption or chemisorption

This process involves electron exchange between the sorbate molecules and the surface of the sorbent, resulting in a chemical reaction. The bond formed between the sorbate and the sorbent is essentially a chemical bond and is stronger than in a physical sorption.

The nature of the forces involved in each of the sorption processes is significantly different. In the physisorption process, no activation energy is required; therefore, the sorption rate is higher even at low temperatures. While chemisorption requires activation energy, the sorption rate is low and depends on the sorption temperature [18].

In the study of new sorbents, it is essential to establish the most appropriate sorption equilibrium correlation, which is indispensable for the reliable prediction of sorption parameters and the quantitative comparison of the sorbent behavior for different sorbent systems, for varied experimental conditions [19].

The most common way to study the behavior of activated carbon is through kinetic and sorption equilibrium models. The first model is related to the study of the kinetics, while the second type is related to the studies of isotherm processes [16].

As a result of activation and carbonization processes, activated carbons with porous characteristics are obtained, which are determined by factors such as starting material, temperatures and carbonization and activation times, heating rate, particle size of the starting material, and so on [12].

In the preparation of an activated carbon, it is necessary to look for the appropriate ratio, as can be deduced from the information earlier, between the transport pores and the sorption pores, that is, it is necessary to achieve a rapid transport of the sorbate to the internal surface and, at the same time, obtain an internal surface sufficiently developed to ensure a high sorbent capacity. In each case, the properties of activated carbon will depend on the raw material, its previous treatment, and activation conditions [17].

Nowadays, a strong demand for activated carbons can be expected in two very important fields in developed countries: atmospheric pollution and wastewater, they are also used for other applications such as elimination of organic matter and toxic substances from industrial gases and drinking water, elimination of chlorine from water, etc. This promising future of activated carbons requires the development of alternative materials that may face the requirement of sorbent materials in the depollution area, especially as regards the search for new raw materials and obtaining very selective activated carbons. Actually, activated carbons with properties like molecular sieve are being prepared in recent years; the object of these materials is the selective sorption of molecules of specific size, a process in which the activated carbons are displacing the zeolites, used frequently for this purpose. Another important application, which takes advantage of the properties of a molecular sieve of activated carbons, is the retention of nitrogen oxides (NOx) from different sources and sulfur that coals and oils contain and that when heated is transformed into toxic products, such as sulfur dioxide (SO_2), hydrogen sulfide (SH_2), carbon sulfide (S_2C), and so on [17].

Recently, fruit husks as agroindustrial waste have been implemented in the production of activated carbons; investigation of sorption about selective specific size molecules has been done regarding these materials. The use of agroindustrial residues is a new alternative that provides a proposal of integral valorization, taking advantage of the waste abundance and the low cost of the material [17].

Table 4 shows the results of some reports from which activated carbons have been elaborated; elaborating parameters as well as surface areas are shown. It is possible to see surface area values from 200 to 1800 m^2/g; these values are comparable to those reported in literature for lignite of 1300 m^2/g [23], as well as 1853 m^2/g [24]. These values are also comparable to commercial materials: PET activated carbons have 1170 m^2/g [25], Darco KB-B of 1608 m^2/g [26], Fluka 05120 of 1110 m^2/g [26], activated carbon MT40 of 528 m^2/g [27], activated carbon BW of 300 m^2/g [27], and Fluka 03866 of 179 m^2/g [26].

4.3. Activated carbons obtained from orange peels

Some studies have been done for the preparation of activated carbon from orange peel, **Table 5** shows some reports and it is possible to appreciate the different activating agents used, temperature, and time of carbonization, as well as the surface area reported for those materials.

Some studies for the elaboration of activated carbons from orange peel are described below; these materials have been used for the removal of metals, dyes, among others. These reports indicate sorption capacities from 7.9 to 982 mg/g.

Quijano and Mejía [31] elaborated activated carbons from the residue obtained after pectin extraction from orange peels; they analyzed the effect of time and carbonization temperature on the carbonization percentage, using a 2^2 factorial design. They determined that temperature has significant influence on the carbonization yield; the optimum condition was obtained at 400°C and 0.5 h for a 34.8% yield and a sorption capacity of methylene blue of 149.4 mg/g.

Annadurai et al. [32] prepared low-cost sorbents from orange peels for the sorption of several dyes in aqueous solution. The concentrations of dye and pH were varied and after the study they determined that sorption capacities decrease as follows: methyl orange > methylene blue > rhodamine B > red congo > methyl violet > black amino 10B, from 20.5 to 7.9 mg/g.

Khaled et al. [33, 34], in different studies, evaluated different conditions to obtain activated carbon; they used H_2SO_4 as an activating agent; a solution of this acid was in contact with the material for 96 h at 105°C; after that, the sample was carbonized at 120°C and 180°C. Obtained activated carbons were evaluated using direct blue dye-106 and direct yellow-12, for which sorption capacities were 107.5 and 75.8 mg/g, respectively.

Material^a	Particle size (mm)	Temperature (°C)	Time (h)	Activation	Agent	Temperature (°C)	Time (h)	Surface area (m^2/g)	Pore volume (cm^3 /g)	Pore size (nm)	Sorption capacity (mg/g)	Reference
Grapefruit	—	450	2	CH	KOH	450, 800	1.5, 2.5	1892.1	1.095	1.92	680	[20]
Banana	—	1000	8		ZnCl	—	—	1650	1.26	3.01	—	[11]
Yaca	—	350	0.5		H_3PO_4	350	0.5	5	—	—	—	[12]
						450	0.5	1033	0.664	1.7	—	
						550	0.5	1260	0.733	2	—	
Almond	1–5	300	1	P	CO_2	—	1	322	19.5	8–12	288.5	[21]
		700	1			—	1	385	16.92	10		
		1200	1			—	1	342	15.5	15–25		
Orange		300	1			—	1	225.6	14.5	7–14	166.7	
		700	1			—	1	248	15	10		
		1200	1			—	1	240	13.5	12–14		
Rice	6×10^{-3}	650	1	CH	NaOH	—	—	253.4	0.17	2.62	0.17	[22]

[a] Materials were considered as the husks of the mentioned fruits. CH: chemical activation and P: physical activation.

Table 4. Organic waste used for the production of activated carbon.

Activation type	Agent	Atmosphere	Temperature (°C)	Carbonization time (h)	Time of mixing material-agent	Surface area (m^2/g)	Reference
Physical	CO_2	Nitrogen	700	1 h	—	248	[21]
Chemical	H_3PO_4	Autogenerated	850	1 h	—	1090	[28]
Chemical	H_3PO_4	Nitrogen	450	2 h	2 h	1203	[29]
Chemical	ZnCl	Nitrogen	550	1 h	36 h	1477	[30]

Table 5. Preparation of activated carbon using orange peels.

Fernandez et al. [35] studied the effect of H_3PO_4 as an activating agent to prepare activated carbon; the carbonization procedure was carried out at 475°C in 0.5 h. Authors report surface areas of 1090 m^2/g for the obtained materials. Methylene blue and rhodamine B were used to characterize sorption capacities and the values obtained were 320 and 522 mg/g, respectively.

Li et al. [20], studied the effect of KOH as an activating agent and the process of carbonization in an inert atmosphere, at 800°C; the activated carbon obtained had a surface area greater than 1800 m^2/g, and a sorption capacity of 680 m/g was obtained using methyl orange as a model pollutant.

Ashtaputrey and Ashtaputrey [36] prepared activated carbon from orange peels by chemical activation using HCl; they also varied the carbonization temperature from 300 to 500°C for 1 h. They analyzed the sorption capacity of iodine, and finally, they concluded that a carbonization temperature of 300°C promotes a sorption capacity of up to 983 mg/g.

5. Preparation and characterization of orange peel-activated carbon

Our results of the preparation of activated carbon from orange peel let us characterize the material. This material was prepared under the following conditions: activation agent, H3PO4, carbonization temperature of 400°C, and carbonization time of 1 h. Methyl orange was used as

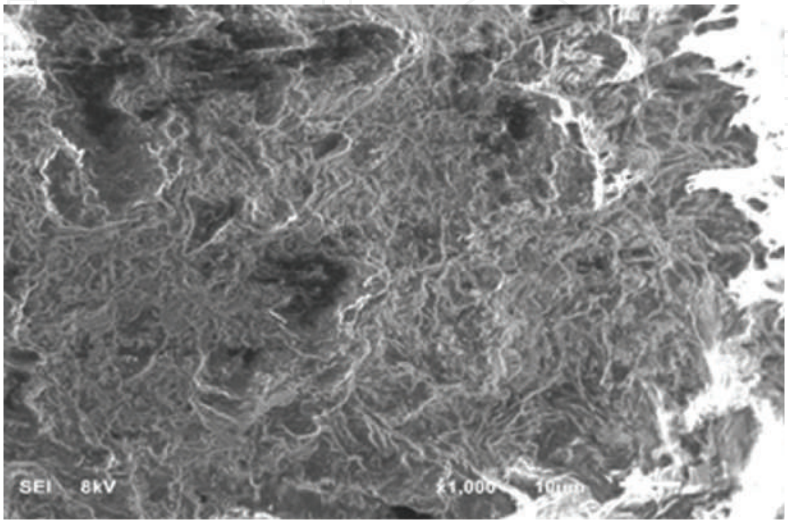

Figure 2. SEM micrography of orange peel at 1000×.

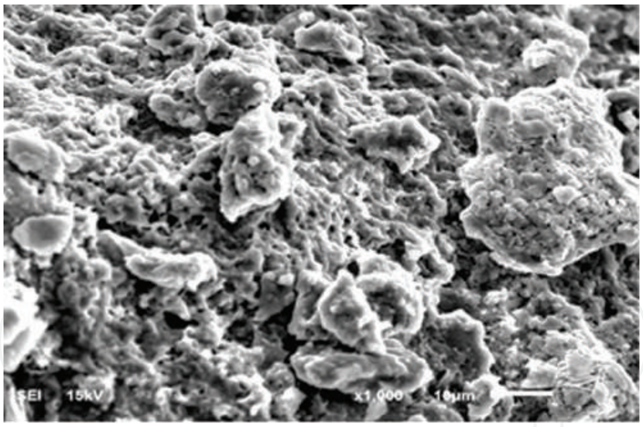

Figure 3. SEM micrography of activated carbon obtained from orange peel at 1000×.

the model pollutant in order to analyze sorption capacity of 2342.91 mg/g. This result was compared to dried orange peel that showed a sorption capacity of 149.26 mg/g.

Figures 2 and **3** show a comparison of the surface morphology of orange peel and activated carbon obtained from orange peel. It can be seen that after the carbonization treatment the surface was modified, given by the thermal process and by the activation agent. The carbonization process promotes the formation of new surface sites.

On the other hand, Fourier Transform Infrared Spectroscopy (FTIR) was used to identify the surface groups of activated carbon obtained from orange peel. **Figure 4** shows the comparison of orange peel and activated carbon. It is possible to appreciate that the intensity of some signals decreases after carbonization process. **Table 6** identifies functional groups associated with the FTIR spectra of **Figure 4**.

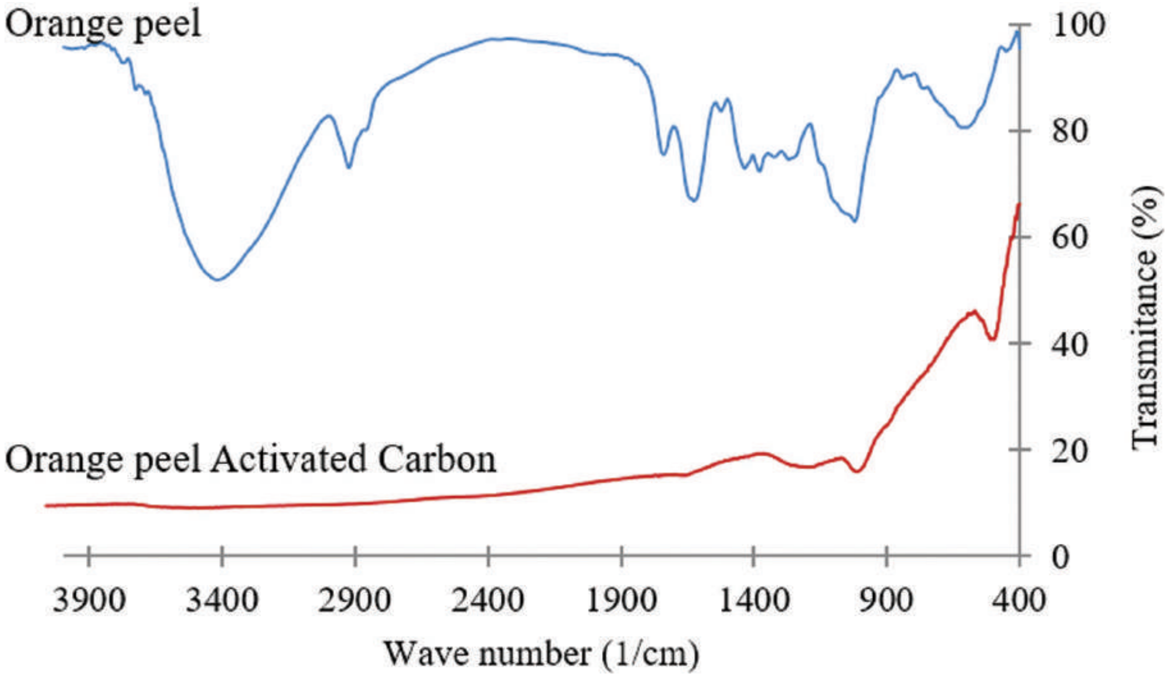

Figure 4. Comparison of the FTIR spectrum of orange peel and orange peel-activated carbon.

Wave number (1/cm)	Functional group
3422.8	—OH
2925.62	C—H
1741.27	C═O
1626.83	C═C
1435.53	$—CH_2$ $—CH_3$ $O—CH_3$
1379.24	C—O
1070	P—O
1020.77	C—O—H C—O—R
596.19	C—H

Table 6. Functional groups of FTIR spectrum.

Activated carbon prepared from orange peel has higher sorption capacity compared to the precursor (dried orange peel), which means that the transformation of a residence is a great advantage. The resulting material possesses the ability to be used for the treatment of water contaminated with colorants as an alternative principal.

However, it is necessary to continue the study of this material for the removal of heavy metals, organochloride compounds, and so on in order to provide greater alternatives for better care for the environment.

6. Sustainable materials

The concept of sustainability arises in 1987, when the World Commission on Environment and Development from the United Nations published a report titled "Our common future" [37], that is focused on the idea of sustainability or sustainable development.

Sustainability is a process that aims to find a balance between the environment and the use of natural resources. Humanity has degraded natural resources in such a way that currently it is necessary to conscientiously procure and plan its consumption to guarantee the existence to future generations.

That is why the use of innovative alternatives for the development of materials allows us to offer better conditions for the care of the environment. Therefore, if a strategy is generated to collect, characterize, and even take advantage of waste materials that currently contribute to the contamination of the environment, in the future, people tend to think of integral use of consumption products. It represents a change in how our society thinks about the use of natural resources and environmental protection.

This is the case of agroindustrial waste, since they have a physicochemical composition that can be used for different purposes, both for the recovery of different raw materials and for their transformation into sustainable materials useful to reduce water pollution.

7. Conclusion

Orange peels are good alternatives as raw materials for the production of activated carbons. Activated carbons obtained from this precursor have high surface areas and high sorption capacities, compared to commercial materials used for water treatment.

Orange peel-activated carbon is a sustainable alternative to replace activated carbons obtained from lignite materials that come from non-renewable sources.

Acknowledgements

Authors thank the Centro de Investigación y Desarrollo Tecnológico en Electroquímica, CIDETEQ (www.cideteq.mx), for the facilities provided for the development of this research.

Author details

Irma Robles Gutierrez*, Ana K. Tovar and Luis A. Godínez

*Address all correspondence to: irobles@cideteq.mx

Center for Electrochemical Science and Technology (CIDETEQ), Pedro Escobedo Queretaro, Pedro Escobedo, Mexico

References

[1] Saval S. Aprovechamiento de residuos agroindustriales: Pasado, presente y futuro. Biotecnología. 2012;**16**:14-46

[2] Luque R, Clark JH. Valorisation of food residues: Waste to wealth using green chemical technologies. Sustainable Chemical Processes. 2013;**1**. DOI: 10.1186/2043-7129-1-10

[3] Comité Sistema Producto Cítricos del Estado de Veracruz. Sagarpa [Internet]. 2009. Available from: http://www.sagarpa.gob.mx/agronegocios/Documents/Estudios_promercado/SISTPROD_CITRICOS.pdf [Accessed: November 2017]

[4] Foreign Agricultural Service. United States Department of Agriculture [Internet]. January 2018. Available from: https://apps.fas.usda.gov/psdonline/circulars/citrus.pdf [Accessed: February 2018]

[5] Castro ME, Sepúlveda A. Estudio de factibilidad técnica y económica de una planta extractora de pectina a partir de los residuos generados por el proceso de industrialización de la naranja (*Citrus sinensis*) [thesis]. Santander: Universidad Industrial de Santander; 2012

[6] Cerón-Salazar I, Cardona Alzate C. Evaluación del proceso integral para la obtención de aceite esencial y pectina a partir de cáscara de naranja. Ingeniería y Ciencia. 2011;**7**(13):65-86

[7] Espachs-Barroso A, Soliva-Fortuny RC, Martín-Belloso O. A natural clouding agent from orange peels obtained using polygalacturonase and cellulase. Food Chemistry. 2005;**92**(1): 55-61. DOI: 10.1016/j.foodchem.2004.04.047

[8] Balu AM, Budarin V, Shuttleworth PS, Pfaltzgraff LA, Waldron K, Luque R. Valorisation of Orange peel residues: Waste to biochemicals and nanoporous materials. ChemSusChem. 2012;**5**:1694-1697. DOI: 10.1002/cssc.201200381

[9] Siles JA, Vargas F, Gutiérrez MC, Chica AF, Martín MA. Integral valorisation of waste orange peel using combustion, biomethanisation and co-composting technologies. Bioresource Technology. 2016;**211**:173-182. DOI: 10.1016/j.biortech.2016.03.056

[10] Miranda R, Bustos-Martineza D, Sosa C, Gutiérrez MH, Rodriguez ME. Pyrolysis of sweet orange (Citrus sinensis) dry peel. Jurnal of Analytical and Applied Pyrolysis. 2009;**86**(2): 245-251. DOI: 10.1016/j.jaap.2009.06.001

[11] Lv y, Gan L, Liu M, Xiong W, Xu Z, Zhu D, Wright D. A self-template synthesis of hierarchical porous carbon foams based on banana peel for supercapacitor electrodes. Journal of Power Sources. 2012;**209**:152-157. DOI: 10.1016/j.jpowsour.2012.02.089

[12] Prahas D, Kartika Y, Indraswati N, Ismadji S. Activated carbon from jackfruit peel waste by H_3PO_4 chemical activation: Pore structure and surface chemistry characterization. Chemical Engineering Journal. 2008;**140**(1–3):32-42. DOI: 10.1016/j.cej.2007.08.032

[13] Álvarez MA, Carrasco F, Maldonado FJ. Desarrollo y aplicaciones de materiales avanzados de carbón. 1st ed. Sevilla|: Universidad Internacional de Andalucía; 2014. 428 p

[14] Marsh H, Rodríguez F, editors. Activated Carbon. 1st ed. Amsterdam: Elsevier; 2006.554 p

[15] Gómez-Serrano V, Piriz-Almeida F, Durán-Valle CJ, Pastor-Villegas J. Formation of oxygen structures by air activation. A study by FT-IR spectroscopy. Carbon. 1999;**37**(10):1517-1528. DOI: 10.1016/S0008-6223(99)00025-1

[16] Kwiatkowski JF, editor. Activated Carbon: Classifications, Properties and Applications. 1st ed. New York: Nova Science Publishers; 2011 572 p

[17] Martinez JMM. Adsorción física de gases y vapores por carbones. 1st ed. Universidad de Alicante; 2009. 116 p

[18] Chand RB, Goyal M. Activated Carbon Adsorption. 1st ed. Boca Raton: CRC Press; 2005. 520 p

[19] Foo KY, Hammed BH. Insights into the modeling of adsorption isotherm systems. Chemical Engineering Journal. 2010;**156**(1):2-10. DOI: 10.1016/j.cej.2009.09.013

[20] Li H, Sun Z, Zhang L, Tian Y, Cui G, Yan S. A cost-effective porous carbon derived from pomelo peel for the removal of methyl orange from aqueous solution. Colloids and Surfaces A: Physicochemical and Engineering Aspects. 2016;**489**:191-199. DOI: 10.1016/j.colsurfa.2015.10.041

[21] Hashemian S, Salari K, Atashi Z. Preparation of activated carbon from agricultural wastes (almond shell and orange peel) for adsorption of 2-pic from aqueous solution. Journal of Industrial and Engineering Chemistry. 2014;**20**(4):1892-1900. DOI: 10.1016/j.jiec.2013.09.009

[22] Mohd TF, Muhammad I, Maizatul S, Chong FK. Adsorptive removal of Zn(II) ion from aqueous solution using rice husk-based activated carbon. In: American Institute of Physics, editor. International Conference on Fundamental and Applied Sciences 2012: (ICFAS2012). American Institute of Physics; 2012. p. 252-257. DOI: 10.1063/1.4757475

[23] Montané D, Torné-Fernández V, Fierro V. Activated carbons from lignin: Kinetic modeling of the pyrolysis of Kraft lignin activated with phosphoric acid. Chemical Engineering Journal. 2005;**106**(1):1-12. DOI: 10.1016/j.cej.2004.11.001

[24] Suhas CPJM, Ribeiro MML. Lignin – From natural adsorbent to activated carbon: A review. Bioresource Technology. 2007;**98**(12):2301-2312. DOI: 10.1016/j.biortech.2006.08.008

[25] László K, Podkościelny P, Dąbrowski A. Heterogeneity of polymer-based active carbons in adsorption of aqueous solutions of phenol and 2,3,4-Trichlorophenol. Langmuir. 2003; **19**(13):5287-5294. DOI: 10.1021/la026761s

[26] Schwickardi M, Johann T, Schmidt W, Schüth F. High-surface-area oxides obtained by an activated carbon route. Chemistry of Materials. 2002;**14**(9):3913-3919. DOI: 10.1021/cm0211857

[27] Podkościelny P, Browski AD, Marijuk OV. Heterogeneity of active carbons in adsorption of phenol aqueous solutions. Applied Surface Science. 2003;**205**(1–4):297-303. DOI: 10.1016/S0169-4332(02)01154-6

[28] Fernandez ME, Nunell G, Bonelli PR, Cukierman AL. Conversión de cáscaras de naranjas en carbón activado y su empleo en el tratamiento de aguas contaminadas por colorantes. In: SAASA, editor. Segundo Simposio sobre Adsorción Adsorbentes y sus Aplicaciones; 2013; SAASA; 2013

[29] Peña KJ, Giraldo L, Moreno JC. Preparation of activated carbon from orange peel by chemical activation physical and chemical characterization. Revista Colombiana de Química. 2012;**41**(2):311-323. DOI: 10.15446/rev.colomb.quim

[30] Xie Z, Guan W, Ji F, Song Z, Zhao Y. Production of biologically activated carbon from orange peel and landfill leachate subsequent treatment technology. Journal of Chemistry. 2014;**2014**:1-9. DOI: 10.1155/2014/491912

[31] Quijano MA, Mejía GM. Integrated utilization of orange peel. Bioresource Technology. 1993;**44**(1):61-63. DOI: 10.1016/0960-8524(93)90209-T

[32] Annadurai G, Juang RS, Lee DJ. Use of cellulose-based wastes for adsorption of dyes from aqueous solutions. Journal of Hazardous Materials. 2002;**92**(3):263-274. DOI: 10.1016/S0304-3894(02)00017-1

[33] Khaled A, El-Nemr A, El-Sikaily A, Abdelwahab O. Removal of direct N Blue-106 from artificial textile dye effluent using activated carbon from orange peel: Adsorption isotherm and kinetic studies. Journal of Hazardous Materials. 2009;**165**(1–3):100-110. DOI: 10.1016/j.jhazmat.2008.09.122

[34] Khaled A, El-Nemr A, El-Sikaily A, Abdelwahab O. Treatment of artificial textile dye effluent containing direct yellow 12 by orange peel carbon. Desalination. 2009;**238**(1–3): 210-232. DOI: 10.1016/j.desal.2008.02.014

[35] Fernandez ME, Nunell GV, Bonelli PR, Cukierman AL. Activated carbon developed from orange peels: Batch and dynamic competitive adsorption of basic dyes. Industrial Crops and Products. 2014;**62**:437-445. DOI: 10.1016/j.indcrop.2014.09.015

[36] Ashtaputrey SD, Ashtaputrey PD. Preparation and characterization of activated charcoal derived from orange peel. Journal of Advanced Chemical Sciences. 2016;**2**(3):360-362

[37] NGO Committee on Education. Report of the World Commission on Environment and Development: Our Common Future [Internet]. 1987. Available from: http://www.un-documents.net/wced-ocf.htm [Accessed: January 2018]